Shock Waves (2021) 31:851–875
https://doi.org/10.1007/s00193-021-01054-2

ORIGINAL ARTICLE

A simplified burn model for simulating explosive effects and afterburning

R. W. Houim[1]

Received: 4 May 2021 / Revised: 15 October 2021 / Accepted: 28 October 2021 / Published online: 15 December 2021

Abstract
A simplified burn model (SBM) was developed for use in simulating the effects of explosive detonations. The goal of SBM is to provide a subgrid model for detonation propagation on grids that are many times coarser than the physical width of the reaction zone. Similar to traditional programmed burn (PB), SBM provides accurate enough initial conditions for simulating large-scale blasts and afterburning processes resulting from the detonation. The governing equations are based on the five-equation compressible multiphase flow model that describes reaction and post-detonation processes similar to reactive burn models. The model uses highly simplified reactant equations of state and reaction rate laws. The reaction model is based on burning rates from traditional PB approaches and is designed to spread the reaction zone over a small number of grid points regardless of the mesh resolution. The detonation velocity and state are independent of the input parameters for the reactant equation of state and reaction model, provided the inputs are physically realistic. The single input parameter for the equation of state must be selected such that the reactant and product Hugoniot curves do not cross, otherwise unphysical weak detonations result. Numerical experiments show that the velocity, state, and bulk structure of Chapman–Jouguet detonations can be reproduced by the model. The resulting blast profiles, pressure–time traces, and detonation velocity for multidimensional simulations are relatively independent on the input parameters, again, provided the inputs are physically reasonable. The simplified burn model shows great potential for simulating afterburning processes with detailed reaction models or explosive particle dispersal. The SBM is relatively straightforward to implement in compressible multiphase flow codes.

Keywords Detonation · Numerical simulation · Multiphase flow · Programmed burn · Reactive burn

1 Introduction

The use of reactive particles to enhance explosive blasts, increase quasistatic overpressure, and produce extended energy release through afterburning processes is an active research topic [1–11]. The detonation of a condensed phase explosive, which may contain energetic particles, is a precursor event to particle dispersal, turbulent mixing, and afterburning processes [12].

In principle, afterburning processes produced by the detonation of an explosive charge can be simulated by fully resolving the detailed structure of the reaction zone and Zeldovich–von Neumann–Döring (ZND) spike of the detonation by using reactive burn approaches [13]. However, such resolution is computationally infeasible due to the large disparity in length scales between the detonation structure and the afterburning fireball. The model for the detonation phase of the explosive material for applications where later-time processes such as afterburning and air blast applications do not have to be as detailed as is required for other applications, such as detonator design [14,15]. Instead, modeling these events requires detailed models for particle transport and collisions, turbulent mixing, and detailed chemical kinetics to describe the late-time dispersal and afterburning processes [11,12]. Resolving details of the detonation structure are not required for these applications. The detonation model for the condensed explosive need only to provide accurate initial conditions for chemical species and particles that may undergo later time dispersal and combustion. This paper presents a simplified burn model (SBM) that can be considered as a subgrid model for condensed phase explosive wave propagation, which satisfies the detonation model require-

Communicated by D. Frost.

✉ R. W. Houim
rhouim@ufl.edu

[1] Department of Mechanical and Aerospace Engineering, University of Florida, Gainesville, FL 32611, USA

ments for afterburning and later-time air blast applications is compatible with multiphase reactive flow models and codes.

The structure of a one-dimensional planar detonation wave predicted by classical Zeldovich–von Neumann–Döring (ZND) theory consists of a shock wave propagating into unburned energetic material followed by a chemical reaction zone. The reactions are autoignition processes initiated by shock compression of the explosive material [16]. The chemical reactions terminate at the Chapman–Jouguet (CJ) point where the reactants have been fully converted into high-pressure and high-temperature products at local thermodynamic equilibrium. The reaction zone between the leading shock wave and the CJ point is often very thin, on the order of 10–100 μm for many explosives and is often impractical to resolve in many large-scale blast and afterburning applications which often have fireball, and blast length scales can be over 10 m.

Reactive burn (RB) models are developed to compute the details of the reaction zone, ZND spike, and transient processes such as shock-to-detonation transition (SDT) [13,17]. Thus, RB models can accurately many transient and multidimensional features, such as corner turning and the formation of "dead-zones" of unreacted explosive material [18]. However, RB models require a calibrated set of input parameters for the reactant equation of state (EOS), product EOS, and reaction rate. Calibration of the reactant EOS and reaction rate requires significant empirical input [19–21], which are unavailable for many materials. RB models require full numerical resolution of the reaction zone of the detonation, which is undesirable and impractical for afterburning applications.

Programmed burn (PB) models forgo the fine details of reactive burn models [15,22,23]. As a result, PB methods can be much more efficient if the overall goal of the computation is to compute the effects of the detonation rather than the detailed detonation structure. Programmed burn models often approximate reaction rate through the use of a burn table that is generated in a preprocessing step to the simulation. The burn table lists the time the detonation arrives at a grid point. The explosive material burn uses a simplified rate law based on a detonation sweeping through a computational cell [24,25]. PB approaches offer enormous flexibility. The burn tables can be based on the Huygens method, where the detonation propagates normal to itself at the CJ velocity (D_{cj}), or account for curvature effects using detonation shock dynamics (DSD) [23]. However, PB approaches are sensitive to fine implementation details. Unphysical phenomena, such as weak detonations, can result if PB is not implemented carefully [15]. In addition, it is not clear how to extend PB methods to multiphase explosives where granular particles can be mixed within the explosive charge or placed in an annular shell surrounding the explosive [12,26].

This paper discusses the development of a simplified burn model (SBM) for simulating blasts, afterburning, and other post-detonation processes. The main objective of the SBM is to provide an approximation for the condensed phase detonation without requiring full resolution of the reaction zone. The SBM is designed compatible with detailed chemical reaction and particulate multiphase models. The SBM can be thought of as a programmed burn approach that is compatible with multiphase and reactive flow models for afterburning.

The overall goals of the simplified burn model are:

1. Approximate detonation propagation using only the thermodynamic state of the reactants (density and enthalpy of formation) and EOS model for the products with minimal additional input parameters (ideally none),
2. Applicable to scenarios that involve multiphase and afterburning processes with particle transport and detailed chemical kinetic models,
3. Produced an approximate detonation pseudo-reaction zone that is resolvable regardless of computational cell spacing, and
4. The detonation can turn corners without a burn table.

To achieve these goals, we combine the formalism of RB approaches with the simplified reaction rate used in the PB approaches. This is possible because the CJ detonation velocity and product state are independent of the reaction model and the reactant equation of state. Thus, RB approaches can be used with any physically reasonable model for the reactant EOS and reaction rate to produce a physically realistic detonation wave. A similar approach has recently been developed [27], but requires several additional input parameters and may not extend easily to multiphase blasts.

The SBM is built on the five-equation compressible multiphase model [28,29], which has been demonstrated in recent reactive burn [20] and SDT simulations [17]. This paper discusses the development of the SBM and the numerical methods used, shows examples of its use, and then compares it with traditional reaction models used in programmed burn. The focus of this paper is on the model for the explosive detonation. Discussions of additional model details for afterburning, including detailed chemical kinetics, multiphase particle dispersal, molecular transport, and turbulence models, will be discussed in follow-on papers. The afterburning model used this paper is highly simplified to place emphasis on the SBM.

2 Model

This section discusses the development of the simplified burn model. First the governing equations are presented. Next, the

equation of state for the products and reactants is discussed. Finally, the reaction model is developed.

2.1 Governing equations

The starting point for the simplified programmed burn model is the reactive Baer–Nunziato (BN) equations. The BN equations are often used to simulate reactive burn and shock-to-detonation transition [30,31]. The BN equations are:

$$\frac{\partial \alpha_\mathrm{h}}{\partial t} + \mathbf{v}_\mathrm{h} \cdot \nabla \alpha_\mathrm{h} = -\dot{\alpha}, \tag{1}$$

$$\frac{\partial \alpha_\mathrm{h}\rho_\mathrm{h}}{\partial t} + \nabla \cdot (\alpha_\mathrm{h}\rho_\mathrm{h}\mathbf{v}_\mathrm{h}) = -\dot{M}, \tag{2}$$

$$\frac{\partial \alpha_\mathrm{g}\rho_\mathrm{g}}{\partial t} + \nabla \cdot \left(\alpha_\mathrm{g}\rho_\mathrm{g}\mathbf{v}_\mathrm{g}\right) = \dot{M}, \tag{3}$$

$$\frac{\partial \alpha_\mathrm{h}\rho_\mathrm{h}\mathbf{v}_\mathrm{h}}{\partial t} + \nabla \cdot (\alpha_\mathrm{h}\rho_\mathrm{h}\mathbf{v}_\mathrm{h}\mathbf{v}_\mathrm{h}) + \nabla \alpha_\mathrm{h} p_\mathrm{h} = p_\mathrm{g}\nabla\alpha_\mathrm{g} - \mathbf{M}, \tag{4}$$

$$\frac{\partial \alpha_\mathrm{g}\rho_\mathrm{g}\mathbf{v}_\mathrm{g}}{\partial t} + \nabla \cdot \left(\alpha_\mathrm{g}\rho_\mathrm{g}\mathbf{v}_\mathrm{g}\mathbf{v}_\mathrm{g}\right) + \nabla \alpha_\mathrm{g} p_\mathrm{g} = -p_\mathrm{g}\nabla\alpha_\mathrm{g} + \mathbf{M}, \tag{5}$$

$$\frac{\partial \alpha_\mathrm{h}\rho_\mathrm{h}E_\mathrm{h}}{\partial t} + \nabla \cdot (\alpha_\mathrm{h}\rho_\mathrm{h}\mathbf{v}_\mathrm{h}H_\mathrm{h}) = p_\mathrm{g}\mathbf{v}_\mathrm{h} \cdot \nabla\alpha_\mathrm{h} - \mathcal{H}, \tag{6}$$

$$\frac{\partial \alpha_\mathrm{g}\rho_\mathrm{g}E_\mathrm{g}}{\partial t} + \nabla \cdot \left(\alpha_\mathrm{g}\rho_\mathrm{g}\mathbf{v}_\mathrm{g}H_\mathrm{g}\right) = -p_\mathrm{g}\mathbf{v}_\mathrm{h} \cdot \nabla\alpha_\mathrm{h} + \mathcal{H}, \tag{7}$$

where subscripts h and g refer to the solid explosive and gas phase, α is the volume fraction, ρ is the density, $\mathbf{v}$ is the velocity vector, p is the pressure, E is the total energy, $\dot{\alpha}$ is the rate of change of the explosive volume fraction due to phase change in the detonation, $\dot{M}$ is the mass rate of phase change, and $\mathbf{M}$ and $\mathcal{H}$ are the momentum and energy exchange between the gas and solid phases. By definition,

$$\alpha_\mathrm{h} + \alpha_\mathrm{g} = 1. \tag{8}$$

The total energy is

$$E = e + \frac{1}{2}\mathbf{v} \cdot \mathbf{v}, \tag{9}$$

where e is the internal energy that includes the enthalpy of formation, Δh_f^0. The BN equations have a long history of success in modeling reactive burn [32–34], shock-to-detonation transition (SDT), deflagration-to-detonation transition [35], etc. The BN equations, however, can be difficult to solve and are computationally intensive due to the non-conservative spatial gradient terms [33,36].

The details of the BN equations, such as separate momentum and energy equations for each phase, are not necessary for programmed burn applications. Here, we make the ansatz that the gas and solid explosive are in homogeneous flow conditions ($\mathbf{v}_\mathrm{h} = \mathbf{v}_\mathrm{g}$) and that they are in mechanical and thermal equilibrium. Thus, the SBM assumes

1. $\mathbf{v}_\mathrm{h} = \mathbf{v}_\mathrm{g} = \mathbf{v}$,
2. $p_\mathrm{h} = p_\mathrm{g} = p$,
3. $T_\mathrm{h} = T_\mathrm{g} = T$.

The mixture mass and energy are defined by:

$$\rho = \alpha_\mathrm{g}\rho_\mathrm{g} + \alpha_\mathrm{h}\rho_\mathrm{h} \tag{10}$$

$$\rho E = \alpha_\mathrm{g}\rho_\mathrm{g}E_\mathrm{g} + \alpha_\mathrm{h}\rho_\mathrm{h}E_\mathrm{h}. \tag{11}$$

Using the mixture definitions and the above assumptions, the BN model reduces to the five-equation multiphase flow model [28,29]. The five-equation model has been used successfully for reactive burn [20] and shock-to-detonation transition [17] simulations. The resulting simplified multiphase governing equation, including species mass transport with chemical reactions, is

$$\frac{\partial \alpha_\mathrm{h}}{\partial t} + \nabla \cdot (\alpha_\mathrm{h}\mathbf{v}) - \alpha_\mathrm{h}\nabla \cdot \mathbf{v} = -\dot{\alpha}, \tag{12}$$

$$\frac{\partial \alpha_\mathrm{h}\rho_\mathrm{h}}{\partial t} + \nabla \cdot (\alpha_\mathrm{h}\rho_\mathrm{h}\mathbf{v}) = -\dot{M}, \tag{13}$$

$$\frac{\partial \alpha_\mathrm{g}\rho_\mathrm{g}}{\partial t} + \nabla \cdot \left(\alpha_\mathrm{g}\rho_\mathrm{g}\mathbf{v}\right) = \dot{M}, \tag{14}$$

$$\frac{\partial \alpha_\mathrm{g}\rho_\mathrm{g}Y_{\mathrm{g},i}}{\partial t} + \nabla \cdot \left(\alpha_\mathrm{g}\rho_\mathrm{g}Y_{\mathrm{g},i}\mathbf{v}\right) = \alpha_\mathrm{g}\dot{\omega}_i + \dot{M}_i \tag{15}$$

$$\frac{\partial \rho\mathbf{v}}{\partial t} + \nabla \cdot (\rho\mathbf{v}\mathbf{v}) + \nabla p = 0 \tag{16}$$

$$\frac{\partial \rho E}{\partial t} + \nabla \cdot [\mathbf{v}\,(\rho E + p)] = 0 \tag{17}$$

where $Y_{\mathrm{g},i}$, $\dot{M}_i$, and $\dot{\omega}_i$ are the mass fraction of production, homogeneous mass rate of production, and heterogeneous rate of production for species i. Mass conservation requires:

$$\dot{M} = \sum_{i=1}^{N_\mathrm{g}} \dot{M}_i, \tag{18}$$

where N_g is the number of gas-phase species. Note that the advection term in the volume fraction transport equation (12), $\mathbf{v} \cdot \nabla\alpha_\mathrm{h}$, is written as $\nabla \cdot \alpha_\mathrm{h}\mathbf{v} - \alpha_\mathrm{h}\nabla \cdot \mathbf{v}$ to reflect how this equation is solved in practice. This manipulation allows for better synchronization of the volume fraction transport with the bulk densities ($\alpha\rho$) for each phase [37,38]. This paper is focused on the simplified model for explosive detonation, which is a necessary component of afterburning. Thus, details such as turbulent mixing, molecular transport models, and particle dispersal are not included in (12)–(17).

2.2 Equations of state

2.2.1 Gas-phase equation of state

The pressure for the gas phase uses a modified Jones–Wilkins–Lee (JWL) equation of state [10,11]

$$p = A\left[1 - \frac{\omega\rho_g}{R_1\rho_0}\right]\exp\left(-R_1\frac{\rho_0}{\rho_g}\right) + B\left[1 - \frac{\omega\rho_g}{R_2\rho_0}\right]\exp\left(-R_2\frac{\rho_0}{\rho_g}\right) + \rho_g R_{\text{mix}} T_g, \quad (19)$$

where A, B, R_1, R_2, and ω are constants and

$$R_{\text{mix}} = Ru\sum\frac{Y_{g,i}}{Mw_i}, \quad (20)$$

Ru is the universal gas constant, $Y_{g,i}$ is the mass fraction of gas-phase species i, and Mw_i is the molecular weight of gas-phase species i. In this formulation, the mixture of JWL model is a thermally perfect equation of state for a mixture of ideal gases with a non-ideal barotropic correction factor to account for the high-pressure gas near the CJ state. This JWL model can easily accommodate multiple species and chemical reactions in the gas phase. Other EOS models such as traditional JWL [39], wide ranging (Davis) [40], and Becker–Kistiakowsky–Wilson (BKW) [41] would be straightforward to adopt.

The gas-phase internal energy is

$$e_g(T_g, Y_{g,i}) = \sum Y_{g,i} e_i(T_g), \quad (21)$$

where e_i is the internal energy for gas-phase species i [42]. The internal energy for each species includes the enthalpy of formation, $\Delta h^0_{f,i}$. This internal energy formulation neglects the real-gas internal energy departure function [43,44] and, as a result, is thermodynamically inconsistent. However, we find that this inconsistent model performs well when predicting realistic post-detonation temperatures. This particular variant of the JWL EOS model has a long history of success in modeling reactive and even multiphase blasts [10–12]. Details on the gas-phase internal energy, specific heat, and input parameters are given in Appendix 1.

The speed of sound of the gas, c_g, is

$$c^2 = c^2_{\text{ideal}} + c^2_n. \quad (22)$$

The ideal sound speed is:

$$c^2_{\text{ideal}} = \gamma R_{\text{mix}} T_g, \quad (23)$$

where

$$\gamma = \frac{Cv_g + R_{\text{mix}}}{Cv_g}, \quad (24)$$

and Cv_g is constant-volume specific heat for the gas mixture. The non-ideal sound speed is:

$$c^2_n = A\left[\left(R_1\frac{\rho_0}{\rho_g} - \omega\right)\frac{1}{\rho_g} - \frac{\omega}{R_1\rho_0}\right]\exp\left(-R_1\frac{\rho_0}{\rho_g}\right) + B\left[\left(R_2\frac{\rho_0}{\rho_g} - \omega\right)\frac{1}{\rho_g} - \frac{\omega}{R_2\rho_0}\right]\exp\left(-R_2\frac{\rho_0}{\rho_g}\right). \quad (25)$$

2.2.2 Reactant equation of state

The goal of the SBM is to provide a subgrid approximation to explosive detonation propagation that functions similar to programmed burn, but is compatible with detailed afterburning models. Accurately capturing details of the ZND spike or reaction zone are not required. Thus, EOS for the explosive can be any model that produces any numerically resolvable ZND spike. The reactant EOS is derived from a Taylor series expansion of the pressure–velocity–density relation obtained by combining mass and momentum Rankine–Hugoniot jump conditions across a shock [39]

$$\rho_0 S = \rho_h u$$
$$\rho_0 S^2 + p_0 = \rho_h u^2 + p,$$

where ρ_0 is the initial density, p_0 is the initial pressure, S is the shock velocity, and u is the particle velocity in the post-shock state. Eliminating u gives

$$p - p_0 = S^2\left(\rho_0 - \frac{\rho_0^2}{\rho_h}\right).$$

Performing a Taylor series expansion of ρ about ρ_0 produces

$$p - p_0 = S^2\left[(\rho_h - \rho_0) - \frac{(\rho_h - \rho_0)^2}{\rho_0} + \cdots\right].$$

Taking the first term gives

$$p - p_0 \approx S^2(\rho_h - \rho_0). \quad (26)$$

This is a linearized pressure–density relation that can be used to define a EOS model if S is a constant. The characteristic shock velocity for a detonation should scale with the Chapman–Jouguet detonation velocity, D_{cj}. Thus, we choose $S = aD_{cj}$, where a is a constant. Substituting this into (26) gives the reactant EOS used for the SBM

$$p - p_0 = a^2 D^2_{cj}(\rho_h - \rho_0). \quad (27)$$

Other reactant equations of state could be used [27,39]. However, other reactant EOS models require several input parameters that are not characterized for many materials. The linearized equation of state only requires a single free parameter a and ρ_0 and D_{cj}, which are typically known for an explosive. Guidelines for choosing a are discussed later.

The internal energy of the explosive, e_h, is determined from thermodynamics of a real gas [43,44]

$$de_\mathrm{h} = Cv_\mathrm{h} dT - \left(p - T \frac{\partial p}{\partial T}\bigg|_v \right) dv. \tag{28}$$

Assuming constant specific heat and evaluating the integral for the reactant EOS give

$$\begin{aligned} e_\mathrm{h} =& \Delta h^0_{f,\mathrm{h}} + Cv_\mathrm{h}\left(T - T_\mathrm{ref}\right) + a^2 D^2_\mathrm{cj} \ln\left(\frac{\rho_\mathrm{h}}{\rho_0}\right) \\ & - \left(p_0 - \rho_0 a^2 D^2_\mathrm{cj}\right)\left[\frac{1}{\rho} - \frac{1}{\rho_0}\right], \end{aligned} \tag{29}$$

where $\Delta h^0_{f,\mathrm{h}}$ is the enthalpy of formation of the explosive reactants at reference temperature T_ref. Specific heat, Cv_h, is added to the internal energy to avoid singular regions in the solution space when performing pressure–temperature equilibration discussed below. The specific heat has no influence on the detonation due to the density being independent of temperature for the linearized reactant EOS model discussed in Sect. 2.3.

The sound speed for explosive reactant is:

$$c^2_\mathrm{h} = a^2 D^2_\mathrm{cj}. \tag{30}$$

The parameter a, in principle, does not affect the CJ state or detonation velocity. However, considering the Zeldovich–von Neumann–Döring (ZND) structure of a detonation [16], we require that

$$\rho_\mathrm{vn} > \rho_\mathrm{cj} > \rho_0, \tag{31}$$

where ρ_vn and ρ_cj are the densities of reactants in the von Neumann spike and products at CJ state, respectively. A Rankine–Hugoniot analysis for an inert shock propagating into the reactants gives

$$\rho_\mathrm{vn} = \frac{\rho_0}{a^2}, \tag{32}$$

$$p_\mathrm{vn} = p_0 + \rho_0 D^2_\mathrm{cj}\left(1 - a^2\right), \tag{33}$$

where p_vn is the value of pressure in the von Neumann spike.

The criterion given in (31) can be stated in terms of Hugoniot curves for the products and shocked reactants [45]. Physically, we require that the reactant and product Hugoniots do not cross and

$$p^\mathrm{H}_\mathrm{prod}(v) > p^\mathrm{H}_\mathrm{react}(v) \;\; \forall \;\; v, \tag{34}$$

where $v = 1/\rho$ and $p^\mathrm{H}_\mathrm{prod}$ and $p^\mathrm{H}_\mathrm{react}$ are the product and reactant Hugoniot curves, respectively.

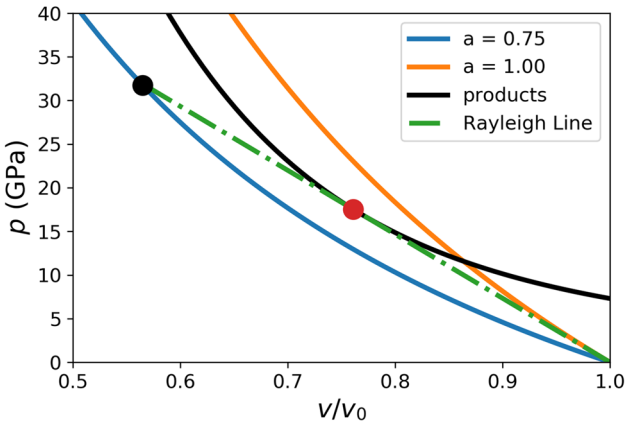

Fig. 1 Rayleigh line and product and reactant Hugoniot curves for values of $a = 0.75$ and 1. The CJ state is indicated by the red dot. The von Neumann point is indicated by the black dot

Figure 1 shows that high values of a produce shock Hugoniots that intersect the product Hugoniot, which leads to unphysical detonations. Lower values of a satisfy (31) and (34). However, values of a that are too low produce unphysically high pressures in the von Neumann spike.

A limiting case for a is when the shock Hugoniot intersects the CJ point

$$a_\mathrm{cj} = \frac{1}{D_\mathrm{cj}} \sqrt{\frac{p_\mathrm{cj} - p_0}{\rho_\mathrm{cj} - \rho_0}}, \tag{35}$$

where p_cj and ρ_cj are the pressure and density at the CJ state, respectively. Applying a safety factor of 0.9 to a_cj to compensate for numerical dissipation in the shock gives $a = 0.76{-}0.79$ for all explosives tested. In practice, we find selecting $a = 0.75$ to be effective. The effect of a on the detonation profiles is discussed below.

2.2.3 Mixed cell treatment

The mixture temperature and pressure are required to close the model and are necessary to compute the pressure gradients and sound speed. The usual EOS inversion procedures are used in regions of pure fluid ($\epsilon < \alpha_\mathrm{h} < 1 - \epsilon$, where $\epsilon = 10^{-6}$) to compute p and T. Mixed cells where both explosive and gas phases are present require an iterative procedure to enforce the mechanical and thermal equilibrium assumptions.

Other simplified approaches are possible to estimate the mixture pressure and temperature [46,47]. However, in general, Arrhenius reaction models for afterburning processes require accurate temperature. Thus, the empirical and less rigorous methods to find the mixture p and T need to be carefully assessed to ensure they do not negatively impact the post-detonation processes.

The pressure and temperature of the mixture are computed by enforcing that the mixture mass and energy

$$\rho = \alpha_g \rho_g + \alpha_h \rho_h, \tag{36}$$
$$\rho e = \alpha_g \rho_g e_g + \alpha_h \rho_h e_h, \tag{37}$$

are the same when based on the conserved variables (α_h, $\alpha_h\rho_h$, and $\alpha_g\rho_g$, ρe) and the EOS models

$$f_1 = \alpha_h \rho_h(p) + \alpha_g \rho_g(p, T) - \rho, \tag{38}$$
$$f_2 = \alpha_h \rho_h(p) e_h(p, T) + \alpha_g \rho_g(p, T) e_g(p, T) - \rho e, \tag{39}$$

where ρ, α_h, and ρe are computed directly from the conserved variables and $\rho_g(p, T)$, $\rho_h(p)$, $e_g(T)$, and $e_h(p, T)$ are computed from the EOS models. (Recall that $E = e + \mathbf{v} \cdot \mathbf{v}/2$.) Newton's method is used to solve for p and T such that $f_1 = f_2 = 0$

$$\begin{bmatrix} P \\ T \end{bmatrix}^{(n+1)} = \begin{bmatrix} P \\ T \end{bmatrix}^{(n)} - \xi \begin{bmatrix} J_{1,1} & J_{1,2} \\ J_{2,1} & J_{2,2} \end{bmatrix}^{-1} \begin{bmatrix} f_1 \\ f_2 \end{bmatrix} \tag{40}$$

where n is the iteration counted. The Jacobian entries are listed in Appendix 2. An under-relaxation factor, ξ, is applied to stabilize the Newton–Raphson iterations

$$\xi = \min(1, \xi_0 \beta^{n-1}), \tag{41}$$

ξ_0 is an initial under-relaxation factor and β is a growth rate. Values of $\xi_0 = 0.1$ and $\beta = 1.01$ work well for most cases. The initial guess values are $p = p_0$ and $T = T_{\text{ref}} = 298$ K. Typically 50 iterations are needed to converge to an error tolerance of 10^{-9}.

A simple volume fraction-weighted mixing rule is used for the sound speed

$$\frac{1}{c_{\text{mix}}^2} = \frac{\alpha_g}{c_g^2} + \frac{\alpha_h}{c_h^2}. \tag{42}$$

The sound speed is used only to compute the time-step size and estimate wave speeds for the approximate Riemann solver. Thus, a simple approximation was found to be sufficient for this work.

2.2.4 Treatment of negative pressure at interfaces

The solid EOS admits negative pressure, which can cause numerical problems in mixed cells where both explosive and gas are present. For example, a solid density of $\rho = 0.9999\rho_0$ is low enough to produce negative pressures in (27). A common scenario where this can occur is when the leading shock of the detonation breaks out of the explosive charge. This produces a strong expansion that is refracted into the solid material. These problem cells are usually burned completely into pure gas before they cause problems. However, if the pressure for the solid EOS is negative, it is not possible for the gas and solid to agree on a common pressure in mixed cells. This often leads to numerical instability and eventually halts the code.

Problematic cells are addressed in a mass conservative manner by adjusting the volume fraction of the solid-phase, α_h (which is not a conserved quantity) in mixed cells such that

$$\alpha_h^{\text{corr}} = \frac{\alpha_h \rho_h}{\rho_{\min}} \quad \text{if} \quad \frac{\alpha_h \rho_h}{\alpha_h} < \rho_{\min} \quad \text{and} \quad \epsilon < \alpha_h < 1 - \epsilon, \tag{43}$$

where $\epsilon = 10^{-6}$ and the values for $\alpha_h\rho_h$ and α_h are taken directly from the conserved variable vector,

$$\rho_{\min} = p_0 \frac{r - 1}{D_{\text{cj}}^2} + \rho_0, \tag{44}$$

and $r = 0.99$. Equation (43) is applied to all mixed cells after every Runge–Kutta stage of the solver.

2.3 Reaction models

2.3.1 Detonation reaction model

The main objective of this work is to develop a simplified model for approximating detonation propagation for the purposes of studying afterburning, air blasts, and other applications. The detonation velocity and CJ state are dependent only on the initial state reactants and the product equation of state. Thus, the model for the detonation reaction rate, $\dot{M}$, can, in principle be any reasonable model. Ignition and growth as well as other reaction models [17,40,48] could be used. However, many of these reaction models require many input parameters. In addition, using these reaction models would require physically resolving the reaction zone of the detonation, in which the SBM is designed to avoid.

The detonation reaction will be physically under-resolved in the SBM. Ideally, the reaction model for $\dot{M}$ will burn all condensed phase materials within a few grid points. Unphysical time-step size-dependent detonation velocities can result the reaction rate being too large [49]. The constraints on the reaction model for SBM are that it is fast enough to produce a detonation structure that is as thin as possible to minimize the number of mixed cells, but is resolvable by the numerical method.

Here we consider a reaction model that is motivated by traditional programmed burn (PB) approaches [24,25]. Consider a detonation wave moving through a computational cell at velocity D_{cj}. The explosive mass consumption rate of a detonation burning through a computational cell for a PB

method is often of the form

$$\dot{M}_{\mathrm{PB}} \sim \rho_{\mathrm{h}} D_{\mathrm{cj}} A/V, \tag{45}$$

where A is a representative surface area of the detonation within a computational cell and V is the volume of the cell. Motivated by $\dot{M}_{\mathrm{PB}}$, reaction rate for the simplified burn model (SBM) is selected to be

$$\dot{M} = \rho_{\mathrm{h}} \dot{\alpha}, \tag{46}$$

where

$$\dot{\alpha} = \begin{cases} \frac{\delta D_{\mathrm{cj}}}{b} & \text{if } (p \geq p_{\mathrm{ign}} \text{ or } T \geq T_{\mathrm{ign}}) \text{ and } \alpha_{\mathrm{h}} > 0 \\ 0 & \text{otherwise.} \end{cases} \tag{47}$$

Here b is a parameter designed to spread the detonation reaction zone over b computational cell widths, p_{ign} and T_{ign} are a pressure and temperature thresholds to begin burning, and δ is a representative area–volume ratio of the detonation in a computational cell

$$\delta = \frac{1}{N_{\mathrm{dim}}} \sum_{i=1}^{N_{\mathrm{dim}}} \frac{1}{\Delta x_i}. \tag{48}$$

Here, N_{dim} is the number of dimensions in the simulation and Δx_i is the grid spacing in direction i. Then, gas-phase species mass production rates are

$$\dot{M}_i = Y_{\mathrm{cj},i} \dot{M} = Y_{\mathrm{cj},i} \rho_{\mathrm{h}} \dot{\alpha}, \tag{49}$$

where $Y_{\mathrm{ci},i}$ is the mass fraction of gas-phase species i at the CJ state. Modification of (47) for use with traditional time-based programmed burn reaction models is discussed in Sect. 9.

Without T_{ign} in (47), refracted release waves form that quench the reaction in the outermost edge of the explosive charge when the leading shock of the detonation breaks out of the solid material. The resulting Khariton layer of unburned solid material is ejected [50]. (See Fig. 2.) Even though the Khariton layer is a physical phenomena that has been observed [50], it is undesirable to attempt to capture it in the proposed SBM. The reaction zone is intentionally much thicker in the SBM approach than it is in physical reality. Thus, the amount of unburned material in the Khariton layer will be grossly overestimated. T_{ign} is used to ensure that all ejected solid materials burn when p falls below p_{ign}, but the temperature is still high. A ignition temperature between 500 and 700 K works well for most applications.

The parameter b spreads the reaction zone over several grid points to avoid numerical instabilities. A value of $b = 2$ is recommended for most cases. The ignition pressure, p_{ign}, is chosen to be high enough to minimize burning in the numerical profile of the leading shock wave. This parameter must also be lower than the constant-volume explosion pressure, p_{cv}. Typically, a value of $p_{\mathrm{ign}} = 2.5$ GPa works well. However, this value may have to be adjusted for non-ideal explosives. The influence of b and p_{ign} is discussed in Sect. 4.

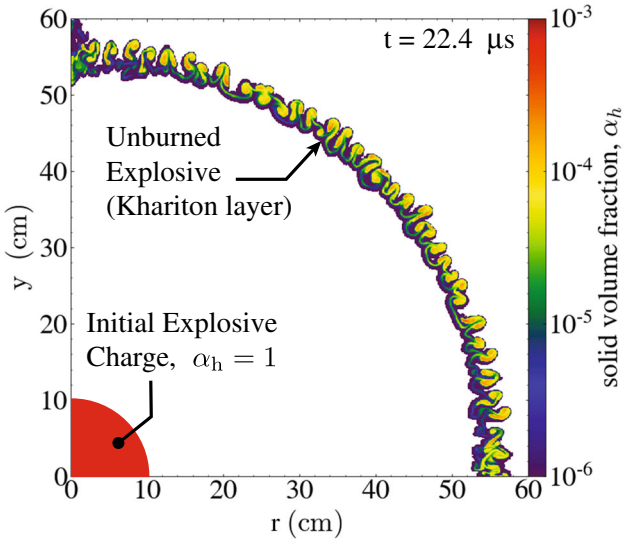

Fig. 2 Unburned explosive ejected by the detonation of a 10-cm-diameter explosive charge when $T_{\mathrm{ign}} = \infty$. The explosive is completely consumed if $T_{\mathrm{ign}} = 500$ K

2.3.2 Ignition of the detonation

The detonation is initiated by defining an "igniter", which is a region inside the explosive that burns at an infinite rate at time t_{ign} (constant-volume explosion limit)

$$\dot{\alpha} = \infty \text{ if } t = t_{\mathrm{ign}} \text{ and } \mathbf{x} \text{ in } \Omega_{\mathrm{ign}}, \tag{50}$$

where $\mathbf{x}$ is the position vector of the computational cell center. Ω_{ign} and t_{ign} are regions occupied by the igniter and its initiation time. The resulting shock from the constant-volume explosion is sufficient to ignite nearby material, provided that $p_{\mathrm{ign}} > p_{\mathrm{cv}}$, where p_{cv} is the adiabatic constant-volume explosion pressure. Numerically, the igniter is implemented by converting all of the solid material into gas at time t_{ign} in Ω_{ign}. This detonation ignition method is flexible enough to accommodate multiple igniters with different shapes and different initiation times.

2.3.3 Homogeneous reactions

The proposed SBM formulation and modified JWL EOS model [10] are flexible enough to accommodate arbitrarily complex chemical reactions necessary to describe explosive afterburning processes. Discussion of afterburning models

with detailed chemical and multiphase reactions will be discussed in a follow-on paper. In this paper, the afterburning proceeds as a single-step irreversible reaction [10]

$$\mathrm{DP} + \nu\mathrm{Air} \rightarrow (1+\nu)\mathrm{AP}, \tag{51}$$

where DP, AP, ν refer to the detonation products, afterburning products, and the stoichiometric mass air–fuel ratio, respectively. The reaction is assumed to proceed at an infinite rate and is mixing limited.

3 Numerical methods and input parameters

Full details of the numerical methods used are given in Appendix 3. The governing equations are solved using the method of lines. A Strang-splitting approach is used to couple the hydrodynamic and the chemical reaction terms. A high-order accurate Godunov algorithm [51] using the fifth-order MUSCL [52,53] scheme is used for spatial discretization. A carbuncle-free version of the HLLC approximate Riemann solver [54,55], HLLC-HLLCM [56], is used to compute the fluxes at the computational cell edges. The governing equations are marched in time using second-order or third-order strong stability preserving Runge–Kutta [57]. The time-step size, Δt, is selected based on the maximum wave speed

$$\Delta t = \frac{\mathrm{CFL}}{\frac{|u|+c}{\Delta x} + \frac{|v|+c}{\Delta y}}, \tag{52}$$

where u and v are the x- and y-velocity components, Δx is the grid spacing in the x-direction, and Δy is the grid spacing in the y-direction.

Adaptive mesh refinement using AMReX [58] is employed to dynamically refine the computational cells near detonations, shocks, and contact surfaces. The code and numerical algorithm have been extensively verified in our earlier work for many test cases including a variety of multidimensional Riemann problems, cellular detonations, Richtmyer–Meshkov instabilities, dust explosions, and flame propagation [36,51,59–61].

Trinitrotoluene (TNT), pentaerythritol tetranitrate (PETN), and tetramethylenetetranitramine (HMX) were used as the explosives for the numerical experiments presented in this paper. The model input parameters for the JWL EOS, reactant EOS, and afterburning stoichiometric air–fuel ratio, ν, are listed in Table 1. Three lumped gas-phase species are used: detonation products (DP), air, and afterburning products (AP). The molecular weights and coefficients for the internal energy polynomials for these species are listed in Appendix 1 [10]. The HMX detonation products use a constant specific heat formulation without afterburning. The numerical experiments presented in the following sections show results for TNT unless stated otherwise.

Table 1 Input parameters and model output states for the constant volume (cv) combustion and Chapman–Jouguet (cj) conditions

	TNT	PETN	HMX[a]
A (GPa)	1576	622.3	778.3
B (GPa)	43.42	20.93	7.071
R_1	6.662	4.935	4.2
R_2	2.158	1.452	1.2
ω	0.4216	0.2689	0.3
ρ_0 (kg/m^3)	1654	1600	1891
Δh_f^0 (MJ/kg)	− 278.3	− 1703	354
Cv_h (kJ/kg K)	1372	1000	1000
ν	3.35	0.482	NA
D_cj (m/s)	6658	7470	9110
p_cj (GPa)	17.5	25.0	45.2
ρ_cj (kg/m^3)	2174	2222	2656
T_cj (K)	3313	4771	9779
p_cv (GPa)	7.3	10.1	16.4
T_cv (K)	2730	4128	6422
ρ_cv (kg/m^3)	1654	1600	1891

The JWL parameters for TNT and ν are from Kuhl et al. [42]. The JWL parameters for PETN and TNT were taken from Dobratz [62]. The enthalpy of formation and condensed phase specific heat were obtained from the NIST Chemistry WebBook [63]

[a]The specific heat of HMX detonation products has a constant value of 1026 kJ/kg

The model output for constant-volume explosion limit and Chapman–Jouguet detonations are listed in Table 1. The CJ state was found by applying the sonic condition of the products and numerically solving the Rankine–Hugoniot conditions [16]

$$\rho_0 D_\mathrm{cj} = \rho_\mathrm{cj} c_\mathrm{cj}, \tag{53}$$

$$\rho_0 D_\mathrm{cj}^2 + p_0 = \rho_\mathrm{cj} c_\mathrm{cj}^2 + p_\mathrm{cj}, \tag{54}$$

$$e_\mathrm{h}(T_0) + \frac{p_0}{\rho_0} + \frac{D_\mathrm{cj}^2}{2} = \sum Y_{\mathrm{cj},i}\, e_{\mathrm{g},i}(T_\mathrm{cj}) + \frac{p_\mathrm{cj}}{\rho_\mathrm{cj}} + \frac{c_\mathrm{cj}^2}{2}, \tag{55}$$

where T_0 is the initial temperature of the explosive, D_cj is the CJ detonation velocity, and c_cj, $Y_{\mathrm{cj},i}$, p_cj, T_cj, and ρ_cj are the product sound speed, the mass fraction of gas-phase species i, pressure, temperature, and density at the CJ state.

4 One-dimensional planar detonations

This section explores the influence of the parameters a, b, p_ign, and the grid spacing on the velocity and structure of one-dimensional planar detonations using the simplified burn

model. The length of the domain was 0.4 m. The detonation is initiated by placing a region of products between $x = 0$ and $x = 2.5$ cm at the constant-volume explosion limit. The baseline case uses $a = 0.75$, $b = 2$, $p_{\text{ign}} = 5$ GPa, and a grid with 1024 computational cells giving $\Delta x = 391\,\mu$m. Adaptive mesh refinement was not used for these 1D numerical experiments. The third-order strong stability preserving Runge–Kutta was used with a CFL number of 0.6 to time-march the governing equations for this 1D parametric study.

4.1 Influence of *a* on the ZND structure

Figure 3 shows the influence of a on the detonation structure, shock Hugoniot, and detonation velocity as a function of time for TNT. Analysis shows that values of $a_{\text{cj}} = 0.87$ give a reactant Hugoniot that intersects the CJ state of the product Hugoniot. A critical value of $a_{\text{crit}} = 0.85$ produces a reactant Hugoniot that is tangent to the product Hugoniot. (See Fig. 3a.)

Examination of the shock Hugoniots shows that cases with $a = 0.75$ and 0.65 produce a von Neumann (VN) spike and satisfy (34). As a result, the ZND structure for these two cases is the classical anvil-shaped pressure profile. The magnitude of the VN pressure is sensitive to the selected value of a, but the bulk structure of the detonation and the Taylor wave following it are insensitive to a, which is the primary goal of the SBM. The details of the reactant EOS do not have any influence on the CJ state and velocity, provided that (34) is satisfied. Thus, the detonation velocity quickly relaxes to D_{cj} for all cases that are able to produce a VN spike.

Cases where $a > a_{\text{cj}} = 0.87$ produce unphysical weak detonations. It is impossible for the detonation to have a ZND structure because the shock and product Hugoniots intersect prior to the CJ state. These detonations produce a broad flat region of supersonic flow between the leading pressure front and the following Taylor wave. For these cases, the pressure front and Taylor wave separate further and further apart as detonation continues to propagate.

Cases where $a_{\text{crit}} < a < a_{\text{cj}}$ could potentially produce CJ detonations. However, the shock and product Hugoniots intersect between the CJ and VN states. As a result, the burning could only be in the weak-burning mechanism discussed above. In fact, we see in Fig. 3b) that the case where $a = a_{\text{cj}} = 0.87$ produced a narrow weak-burning region where the pressure profile is flat. The case where $a = a_{\text{crit}}$ produced a CJ detonation without the VN spike, but this value of a causes problems in multidimensional rate-stick simulations discussed in Sect. 5.

4.2 Influence of *b* on the ZND structure

The influence of the reaction zone spreading parameter, b, on the ZND structure and detonation velocity is shown in Fig. 4. Here we choose $a = 0.75$ and $a = 1$ to examine the influence of reaction model parameters on the velocity and structure of CJ and weak-burning detonations.

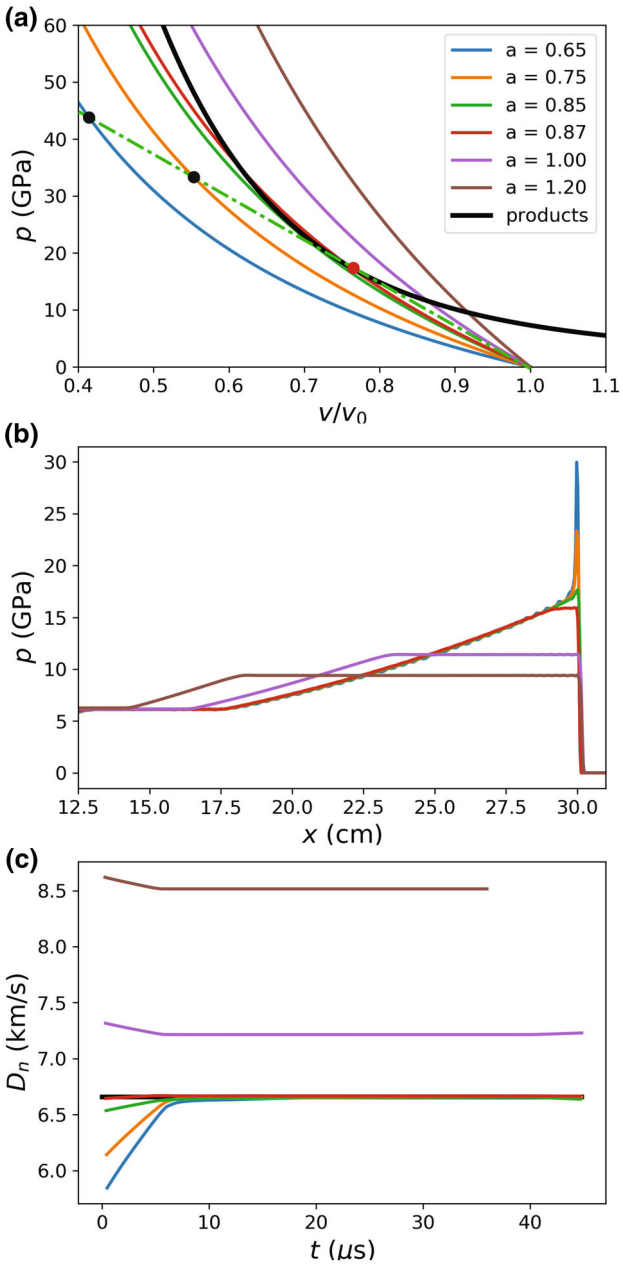

Fig. 3 Influence of a on **a** shock Hugoniot curves, **b** detonation structure, and **c** detonation velocity, D_{n} for TNT. The Rayleigh line in (**a**) is the green dash-dot line. The red and black dots are the CJ and von Neumann states, respectively. The CJ detonation velocity is indicated by the black line in (**c**). The values of b and p_{ign} were 2 and 5 GPa, respectively

The selection of b does not have an influence on the detonation velocity or the overall ZND structure of the detonation and Taylor wave. The only relatively minor influence is that the peak numerical shock pressure asymptotes towards the

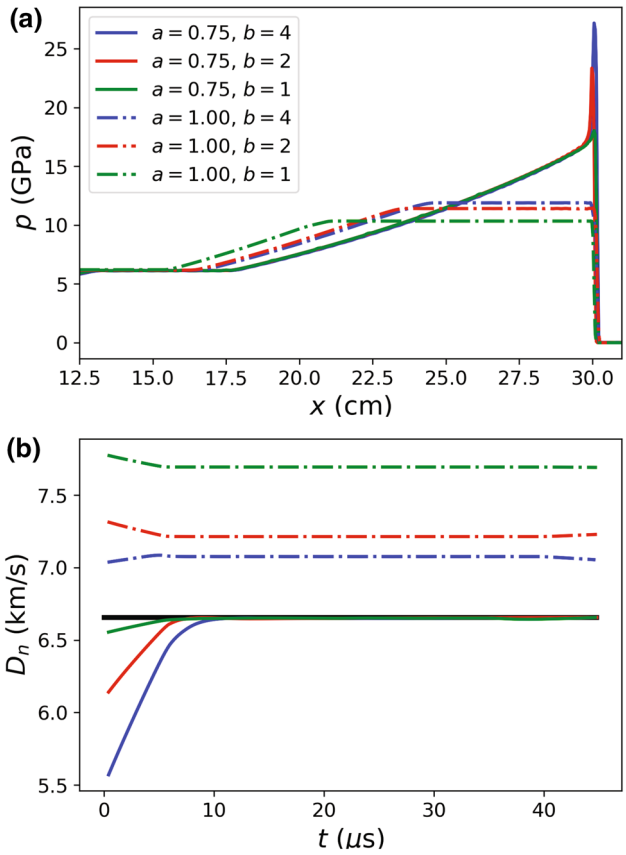

Fig. 4 Influence of b on **a** detonation structure and **b** detonation velocity, D_n for TNT. The CJ detonation velocity is indicated by the black line in (**b**). The value of p_{ign} is 5 GPa

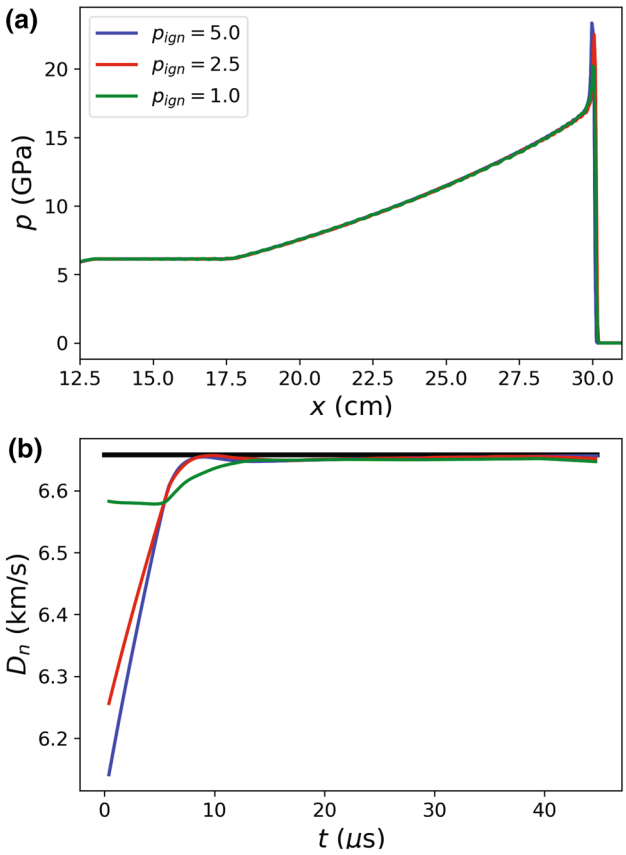

Fig. 5 Influence of p_{ign} on **a** detonation structure and **b** detonation velocity, D_n for TNT. The CJ detonation velocity is indicated by the black line in (**b**). The values of a and b were 0.75 and 2, respectively

VN state as b increases. Low values of b burn more material within the numerically diffused shock profile, which, in turn, expands the flow inside the shock and lowers the peak shock pressure. However, all other detonation output parameters are unaffected by the choice of b. This is expected behavior because the CJ state and D_{cj} are independent of the reaction model.

4.3 Influence of p_{ign} on the ZND structure

The influence of the reaction initiation pressure, p_{ign}, on the ZND structure and CJ velocity is shown in Fig. 5. In all cases, the detonation velocity propagates at D_{cj}. The influence of p_{ign} is similar to the influence of b as only the peak shock pressure is influenced. Decreasing p_{ign} increases the amount of burning within the leading shock, which, as stated above, lowers the peak shock pressure.

4.4 Influence of grid refinement on the ZND structure

Figure 6 shows the influence of grid refinement on the structure and the detonation velocity as a function of time. Overall, the structure of the detonation and Taylor waves are not significantly influenced by grid refinement. However, the width of the ZND spike does change with grid resolution. The parameter b is designed to spread the reaction zone over b cell-widths regardless of the grid. Thus, the width of the reaction zone is directly proportional to computational cell size, Δx, which is shown in Fig. 6. The peak shock pressure is nearly identical for all grids. The grid spacing also has a slight impact on how quickly the detonation relaxes toward D_{cj}. The detonation has to propagate for a longer amount of time for it to become completely independent of the initial conditions as the grid becomes coarser.

5 Multidimensional rate-stick detonations

The performance of the simplified burn model (SBM) on an uncased rate-stick is examined. The diameter and length of the cylindrical charge (rate-stick) are 10 cm and 1 m, respectively. The governing equations are solved two-dimensional axisymmetric (x–r) coordinates. The domain is 1 m in length and has an outer radius of 50 cm. Adaptive mesh refinement

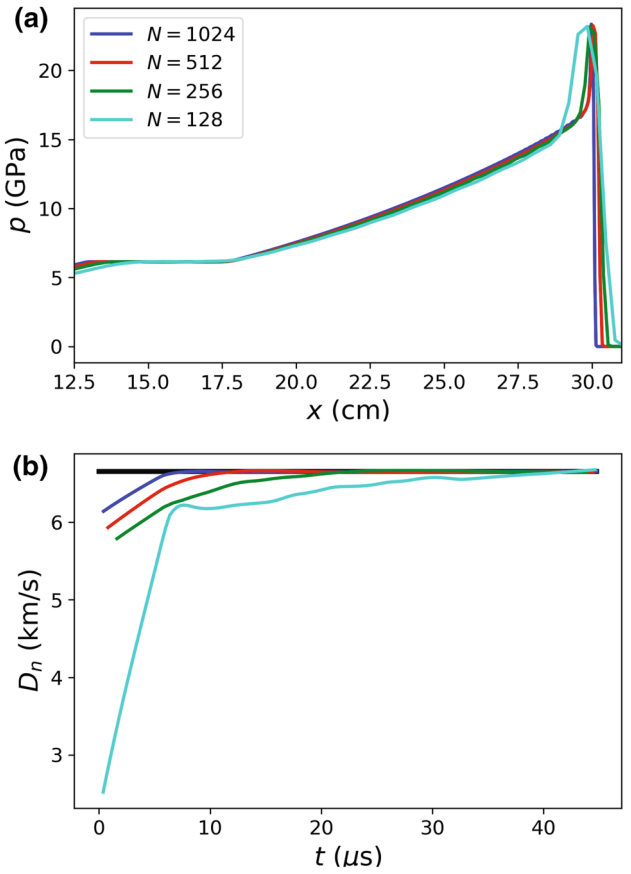

Fig. 6 Influence of the number of grid refinement on **a** detonation structure, and **b** detonation velocity, D_n for TNT. The CJ detonation velocity is indicated by the black line in (**b**). The values of a, b, and p_{ign} where 0.75, 2, and 5 GPa, respectively

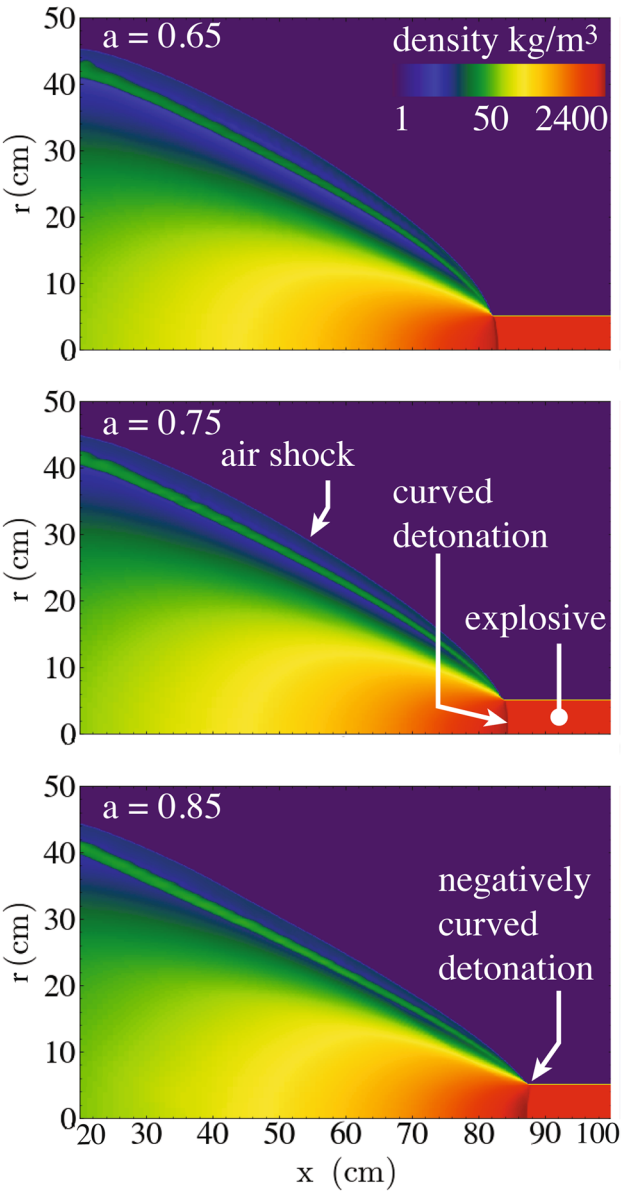

Fig. 7 Influence of a on the detonation and air shock produced by the detonation of a cylindrical charge. The values of b and p_{ign} are 2 and 2.5 GPa, respectively

is used with 4 levels of refinement on a base grid of 128 and 64 cells in the axial (x) and radial (r) directions, respectively. This gives an effective resolution of 1024 by 512 computational cells with $\Delta x = 977\,\mu$m. The baseline parameters are $a = 0.75$, $b = 2$, and $p_{ign} = 2.5$ GPa. The charge is initiated by placing an ignition region with a diameter of 10 cm (the charge diameter) between $x = 0$ and $x = 2.5$ cm. The second-order Runge–Kutta scheme is used to time-march the governing equations with CFL $= 0.8$ to a final time of $t = 125\,\mu$s.

5.1 Influence of *a* on rate-stick detonations

Figures 7 and 8 show the influence of a on the detonation structure velocity, respectively, on the rate-stick. The overall structure of the detonation and air shock fairly typical of a rate-stick [13]. The high-pressure products produced by the detonation drive an oblique shock that propagates into the air. A reactive shear layer forms at the interface between the detonation products and shock-heated air.

The detonation profiles are slightly curved in Fig. 7. The influence of the curved detonations and different VN states as a function of a produce slightly different air shock profiles very close to the explosive. The propagation velocity of the detonation asymptotes to values less than D_{cj} when $a < a_{crit}$. It is well known from detonation shock dynamics (DSD) theory [23] that the velocity of a curved detonation is a function of curvature through a D_n-κ relation (κ is the detonation curvature). Thus, the dependence of D_n on a and other parameters is expected due to the influence of the reaction zone on detonation curvature. However, the effect of this curvature is slight and D_n is around 3% lower than D_{cj} when $a = 0.65$ and 1% lower when $a = 0.75$.

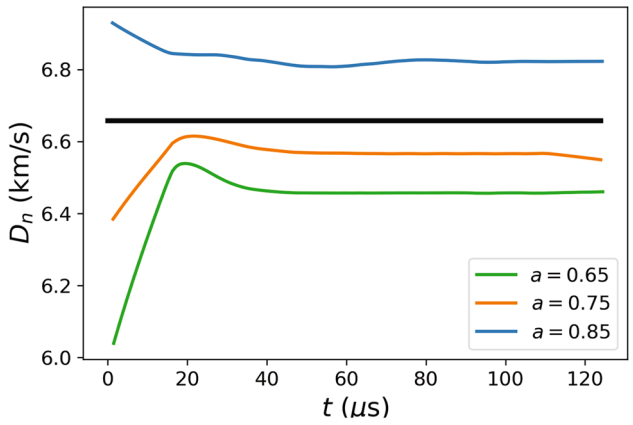

Fig. 8 Influence of, a, on the detonation velocity of a cylindrical charge. The values of b and p_{ign} are 2 and 2.5 GPa, respectively

The case where $a = a_{\text{crit}} = 0.85$ was a limiting case that produced a CJ detonation without a von Neumann spike in the 1D configuration. However, $a = 0.85$ case produces unphysical results for the rate-stick configuration. This detonation has negative curvature shown in Fig. 7. This causes the D_{n} to increase from D_{cj}. This is a completely unphysical result for an uncased explosive charge.

5.2 Influence of *b* on rate-stick detonations

Figure 9 shows the influence of the reaction zone spreading parameter, b, on the structure of the detonation and air shock. Figure 10 shows the influence of b on the detonation velocity, D_{n}, for the rate stick.

The results show that the curvature of the detonation increases slightly with increasing b. The case where $b = 2$ has slight curvature, while the case where $b = 8$ has much more curvature. Cases with wider reaction zones allow expansion waves generated at the explosive-air interface from the detonation interaction to have a greater impact on the detonation curvature. As a result, the influence of increased curvature has an impact on D_{n}.

A case where $b = 1$ was also performed, but not shown. This case produced unphysical results where D_{n} was significantly greater than D_{cj}. The reaction zone is only one computational cell wide. This is well known to produce unphysical results that are dependent on the time-step size and numerical implementation details [49]. Setting $b \geq 2$ solves this issue. Selecting $b \leq 1$ cannot be recommended.

5.3 Influence of grid refinement on rate-stick detonations

Figures 9 and 12 show the impact of grid refinement on the detonation structure and velocity for the rate-stick scenario. Grid refinement was altered by changing the maximum

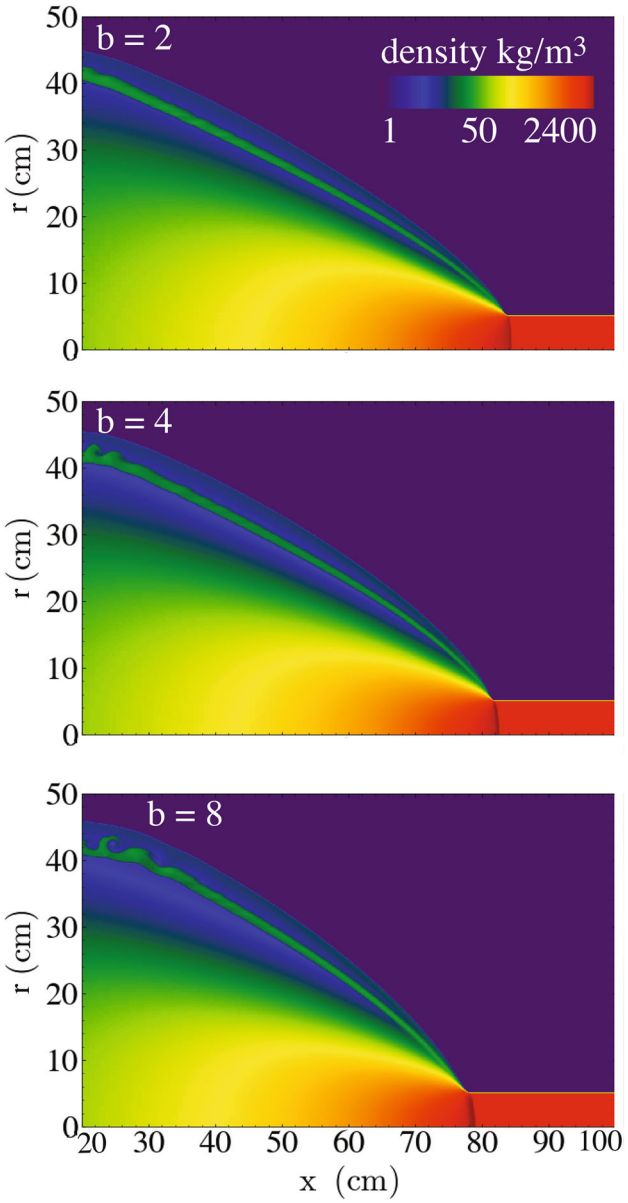

Fig. 9 Influence of the reaction zone spreading parameter, b, on the detonation and air shock produced by a cylindrical charge. The values of a and p_{ign} are 0.75 and 2.5 GPa, respectively

refinement level of the adaptive grid. The coarse, baseline, and fine grids used 3, 4, and 5 levels of refinement respectively. The effective resolution was $\Delta x = 1.95$, 0.977, and 0.488 mm, for the coarse, medium, and fine grids.

The results in Fig. 11 show that the overall structure of the detonation and air shock are very close for all three grid resolutions. There are some slight differences related to the influence of detonation curvature caused by the changing reaction zone thickness with the computational grid size. As a result of the changing curvature, the detonation velocity is slightly influenced by grid resolution. However, the differ-

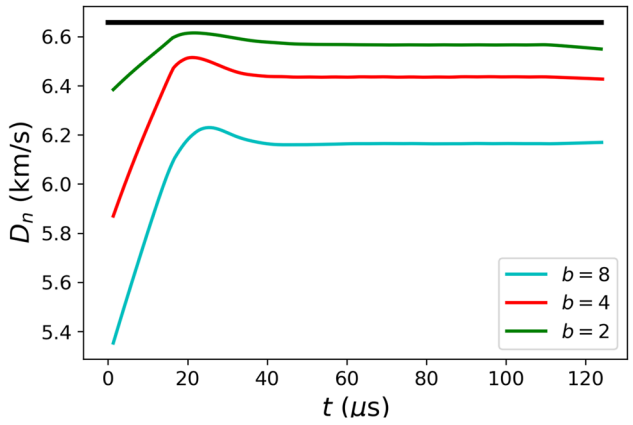

Fig. 10 Influence of, b, on the detonation velocity of a cylindrical charge. The values of a and p_{ign} are 0.75 and 2.5 GPa, respectively

ence between D_{cj} and D_n is only around 2.2% for the coarse grid, which is sufficient for most applications (Fig. 12).

The parameters b and Δx have similar influences on D_{n}. This is observed by carefully examining Figs. 10 and 12. Doubling b or Δx doubles the difference between D_{n} and D_{cj}. This can be explained by reaction rate, (47), which is proportional to $\delta/b \sim 1/(b\Delta x)$. Thus, forcing $b\Delta x$ to be constant under grid refinement should, in principle, produce grid independent D_{n}. However, recall that the SBM is designed to produce a detonation that is b computational cells wide regardless of resolution. This is to avoid unphysical numerical issues when the reaction zone is too thin as discussed above. The differences between D_{n} and D_{cj} are fairly small even on coarse grids, which is likely sufficient for most air blast and afterburning scenarios, which the proposed SBM is developed to address. In scenarios where the propagation velocity of the detonation must exactly be D_{cj} time-based ignition criterion can be used rather than the pressure-based ignition criterion in (47). This modification to the reaction models is discussed in Sect. 9.

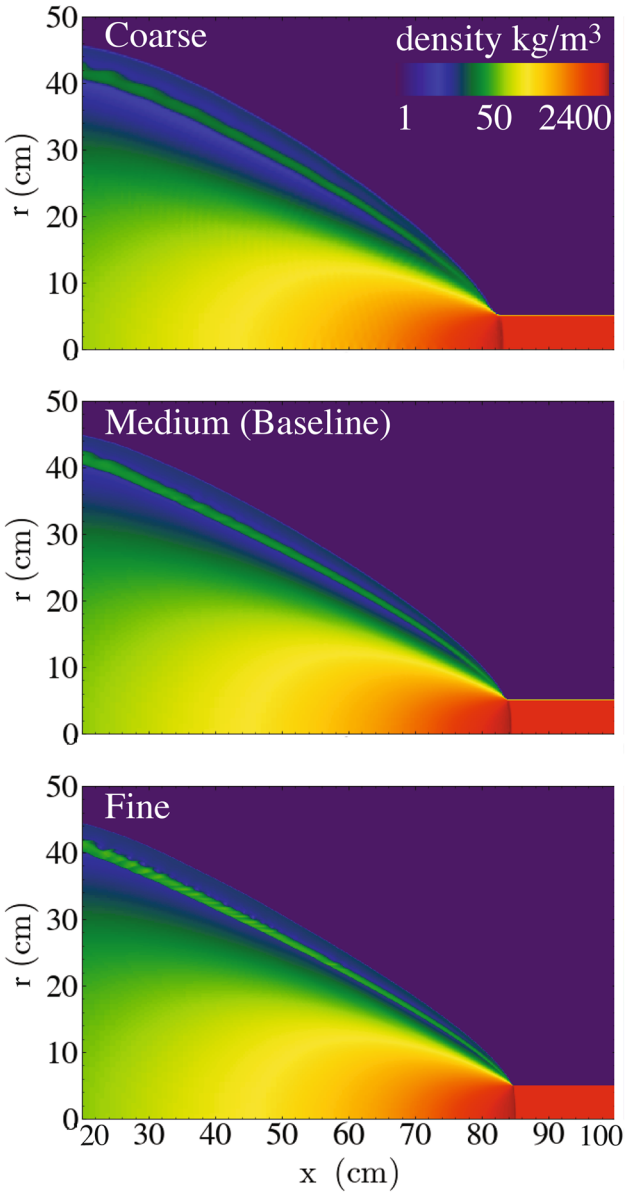

Fig. 11 Influence of grid refinement on the detonation and air shock produced by a cylindrical charge. The grids used $\Delta x = 1.95$ mm (coarse), 0.977 mm (baseline), and 0.488 mm (fine). The values of a, b, and p_{ign} are 0.75, 2, and 2.5 GPa, respectively

6 Spherical air blast

The influence of a on the blast produced by a spherical 20 cm-diameter explosive charge is explored. The charge is center-initiated by placing a 2 cm-diameter ignition region of detonation products at the constant-volume explosion limit. The governing equations are solved in 2D axisymmetric (r–y) coordinates. The domain measures 1 m by 1 m. Five levels of adaptive mesh refinement are used, providing an effective resolution of $\Delta x = 488\,\mu$m. The solution is time-marched to 300 μs using second-order Runge–Kutta with CFL = 0.8. Values of 2 and 2.5 GPa are used for b and p_{ign}, respectively.

Figure 13 shows the density field produced by the detonation of spherical charge at 300 μs. The detonation of the charge produces an expanding blast, a left-running secondary shock, and a reactive contact surface between the shock-heated air and the fuel-rich detonation products. All three values of a that were considered produce very similar results on the blast. The positions of the air and secondary shocks are nearly identical for all three cases. There are some subtle differences in the details of the fireball surface that likely caused by differences in the magnitude of the von Neumann spike. Differences in pressure magnitude and shock strength in the

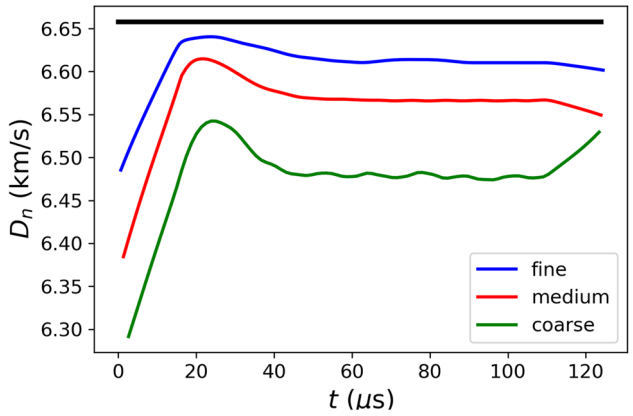

Fig. 12 Influence of grid refinement the detonation velocity of a cylindrical charge. he grids used $\Delta x = 1.95$ mm (coarse), 0.977 mm (baseline), and 0.488 mm (fine). The values of a, b, and p_{ign} are 0.75, 2, and 2.5 GPa, respectively

explosive material can have an impact on the development of Rayleigh–Taylor and Richtmyer–Meshkov instabilities that form on the surface of the fireball [64]. Nevertheless, these differences are small and do not affect the overall dynamics of the blast or afterburning processes.

Figure 14 shows the pressure-time traces measured at radial locations of 0.14, 0.35, and 0.71 m along 45° ray measured from the y-axis. The timing and magnitude of pressure-time traces for all three cases are close.

7 Corner turning

In this section, the simplified burn model is used on a complex-shaped explosive to demonstrate corner turning and the resulting complex blast structure. Any reaction model that is based on a pressure or temperature sensitive reaction model with a physically reasonable condensed phase EOS, such as the SBM, will have the ability to turn corners. Programmed burn or similar time-based reaction models will require a burn table to turn corners. The SBM is an approximation that can allow the detonation to turn corners without the use of a burn table. Nevertheless, the SBM, due to its design and intended applications, cannot accurately capture the detonation curvature effects or the formation of dead zones. More rigorous reactive burn models (or burn tables based on DSD theory) are recommended for simulating chargers with severe corner turning. Thus, the results presented in this section are an extreme and qualitative demonstration showing that the SBM can turn corners.

An asterisk-shaped TNT charge is created with three rectangles 5 cm in width and 25 cm in length centered at the origin. The rectangles are rotated by angle $\theta_i = 60°(i-1)$ from the x-axis, where i is the rectangle number. The charge is initiated by placing a 2 cm-diameter igniter region at the left side of the charge. The shape of the charge, rectangle number, and igniter location are shown in Fig. 15 at $t = 0\,\mu$s.

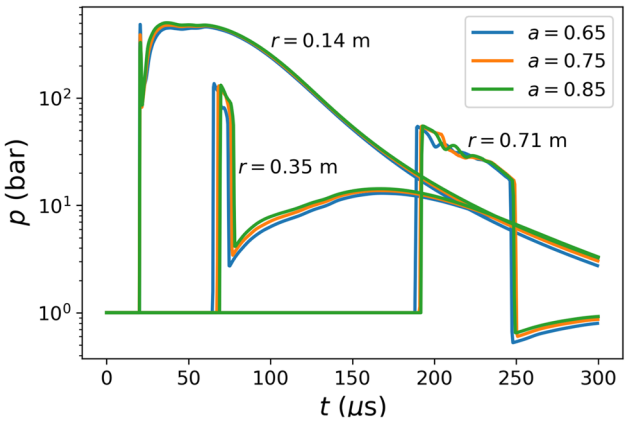

Fig. 14 Pressure-time traces recorded at $r = 0.14$, 0.35, and, 0.71 m at a 45° angle measured from the y-axis

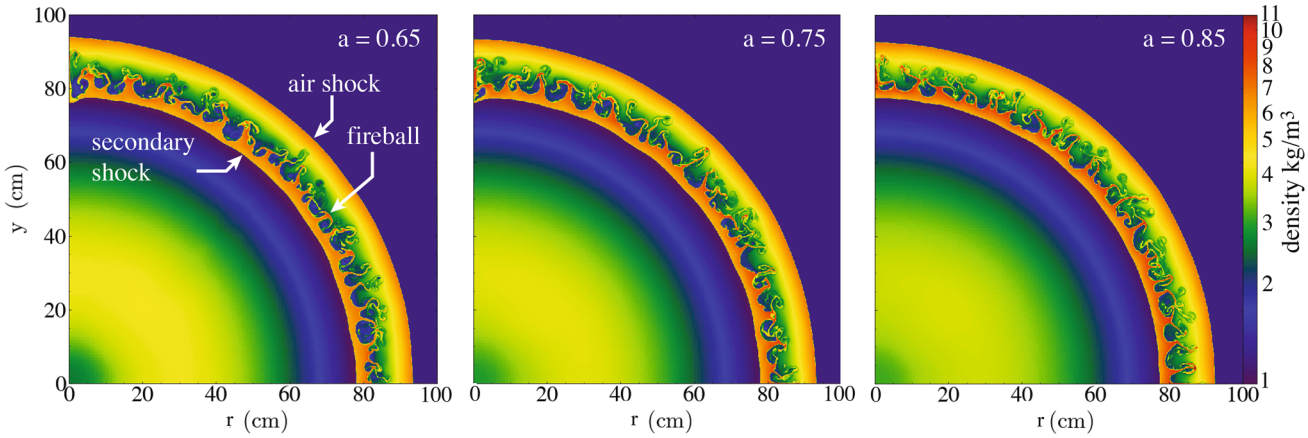

Fig. 13 Influence of a on the blast at 300 μs produced by a hemispherical 20 cm-diameter explosive charge

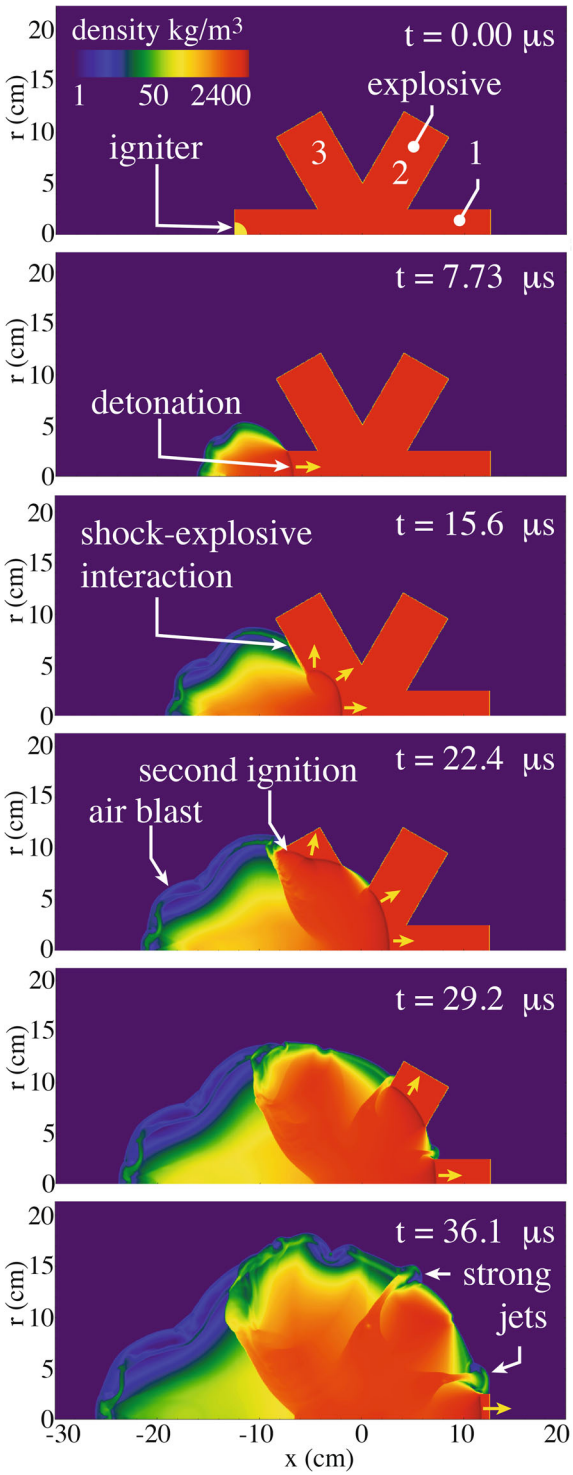

Fig. 15 Time sequence of the mixture density of a detonation propagating through a complex-shaped TNT charge. The time of each image is displayed on the upper-right corner. The propagation direction of the detonation at each time is indicated by the yellow arrows. The numbers on the uppermost image indicate the rectangle number

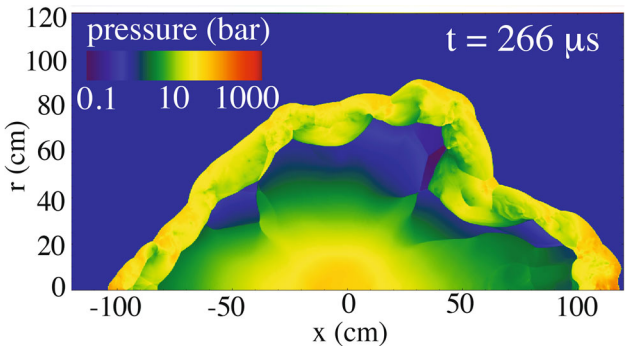

Fig. 16 Pressure field produced by the detonation of the complex charge at 266 μs

The governing equations are solved in 2D axisymmetric (x–r) coordinates. The domain measures 2.4 m by 2.4 m. Five levels of refinement are used with an effective resolution of $\Delta x = 596\,\mu$m, which correspond to a 4096 by 4096 grid at maximum refinement. The solution is time-marched using second-order Runge–Kutta with CFL = 0.8. Values of 0.75, 2, and 2.5 GPa are used for a, b, and p_{ign}, respectively.

Figure 15 shows a time sequence of the mixture density. Initially a detonation propagates to the right from the igniter region in rectangle 1. This produces a blast and detonation structure is similar to the rate-stick problem discussed above. At 15.6 μs, the detonation spreads out into rectangle 3 of the charge as it continues propagating. At 22.4 μs, the detonation continues propagating through rectangles 1 and 3 and begins propagating into rectangle 2. As time increases, the detonation continues propagating into the remainder of the charge. The interaction of the blasts produced by the detonation propagating through the nearby rectangles produces strong jets. This results in a complex blast structure at later times shown in Fig. 16.

Figure 15 shows that a shock-explosive interaction occurs at 15.6 μs where the blast from rectangle 1 impacts rectangle 3. The numerical method and model are robust enough to handle this challenging interaction of a strong shock with a large jump in density at an interface between the gas and explosive. However, this shock-explosive interaction initiated a second detonation that is shown by kinked detonation profile at 22.6 μs. The second detonation ignites due to shock compression increasing the temperature above T_{ign} (500 K) in (47) in the mixed air and explosive cells near rectangle 3. Increasing T_{ign} to 700 K avoids this second ignition as shown in Fig. 17, but is still low enough to burn the ejected material in the Khariton layer. Accurate simulation of shock-induced reactions in an explosive charge is well beyond the scope of the SBM and requires the use of more complex reactive burn models. Thus, the second ignition is undesirable behavior for the SBM. Nevertheless, this interaction demonstrates that the

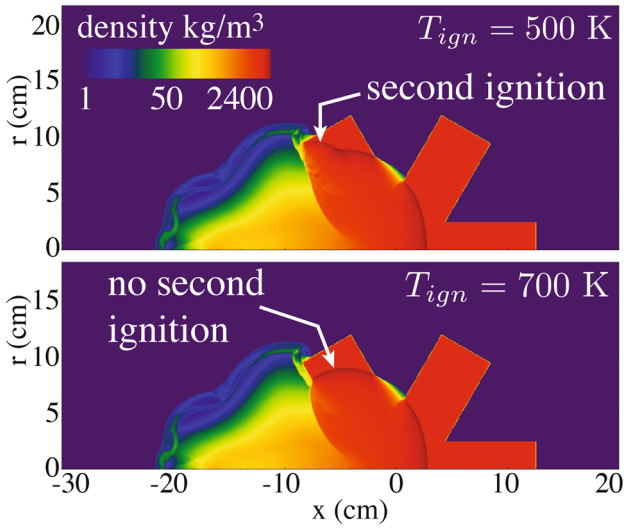

Fig. 17 Mixture density field showing in the influence of T_{ign} on the initiation of secondary detonations from shock-explosive interactions on charges with non-convex geometry at 22.4 μs

SBM and P-T equilibration procedure are robust enough to handle such interactions.

8 Influence of explosive material on the ZND structure

The previous sections presented results using TNT as the explosive material. This section presents results using PETN and HMX as the explosive compound and compares them.

Figures 18 and 19 show the Hugoniot curves, ZND structure, and the ratio of D_{n} to D_{cj} for HMX, PETN, and TNT. A value of $a = 0.75$ was used for all cases. The value of 0.75 for a is capable of producing a valid von Neumann spike and a physically realistic ZND wave structure that propagates at the correct CJ detonation velocity for all three explosive materials.

Figure 20 shows cylindrical air shock structure produced by PETN, HMX, and TNT. The results show that the SBM is robust for multidimensional configurations for all three explosives considered.

9 Comparison of SBM to traditional programmed burn

The simplified burn model was developed to be used as a substitute for programmed burn (PB) models that are compatible with multiphase reactive flow solvers. The previous results show that the SBM works effectively as a PB model for applications where the detailed structure of the reaction zone is not a primary concern. However, there are slight curvature effects that can change the normal detonation velocity (D_{n}) in the rate-stick configuration. D_{n} reduced by 1% to 4% for various combinations of a, b, and p_{ign}. Even though this reduction in D_{n} is small, it may be undesirable in some applications.

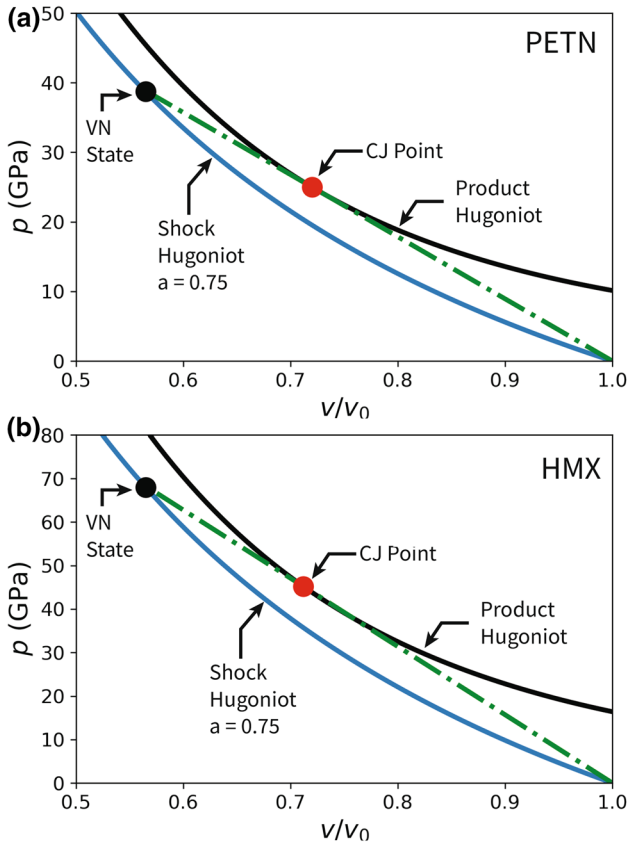

Fig. 18 Shock and product Hugoniot curves for **a** PETN and **b** HMX using $a = 0.75$

The SBM can be transformed to function very similarly to a traditional PB model by changing the pressure-based ignition criterion in (47) to a time-based ignition criterion

$$\dot{\alpha} = \begin{cases} \frac{\delta D_{\text{cj}}}{b} & \text{if } t \geq t_{\text{ign}} \text{ and } \alpha_{\text{h}} > 0 \\ 0 & \text{otherwise,} \end{cases} \tag{56}$$

where t is the solution time and t_{ign} is the time of arrival of the detonation. The time of arrivals can be determined using formal burn tables based on detonation shock dynamics (DSD) [22], or simple Huygens propagation rules. For example, the time of arrival for point initiation using the Huygens rule would be

$$t_{\text{ign}} = \frac{|\mathbf{x} - \mathbf{x}_{\text{ign}}|}{D_{\text{cj}}}, \tag{57}$$

where $\mathbf{x}$ and $\mathbf{x}_{\text{ign}}$ are the position vectors of the cell center and the initiation point, respectively. Details of the integra-

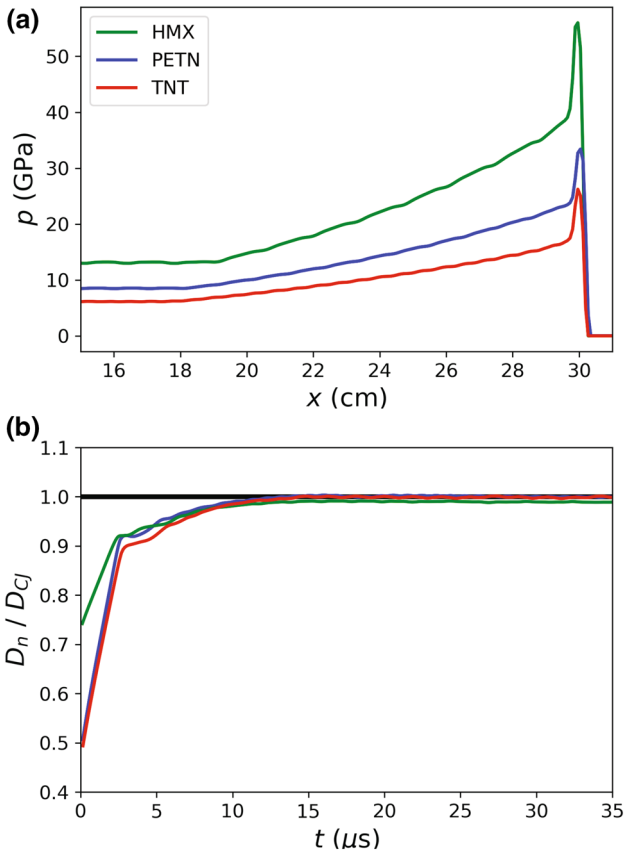

Fig. 19 The **a** ZND structure and **b** Dn/D_{cj} for TNT, HMX, and PETN using $a = 0.75$, $b = 2$, and $p_{\text{ign}} = 2.5$ GPa

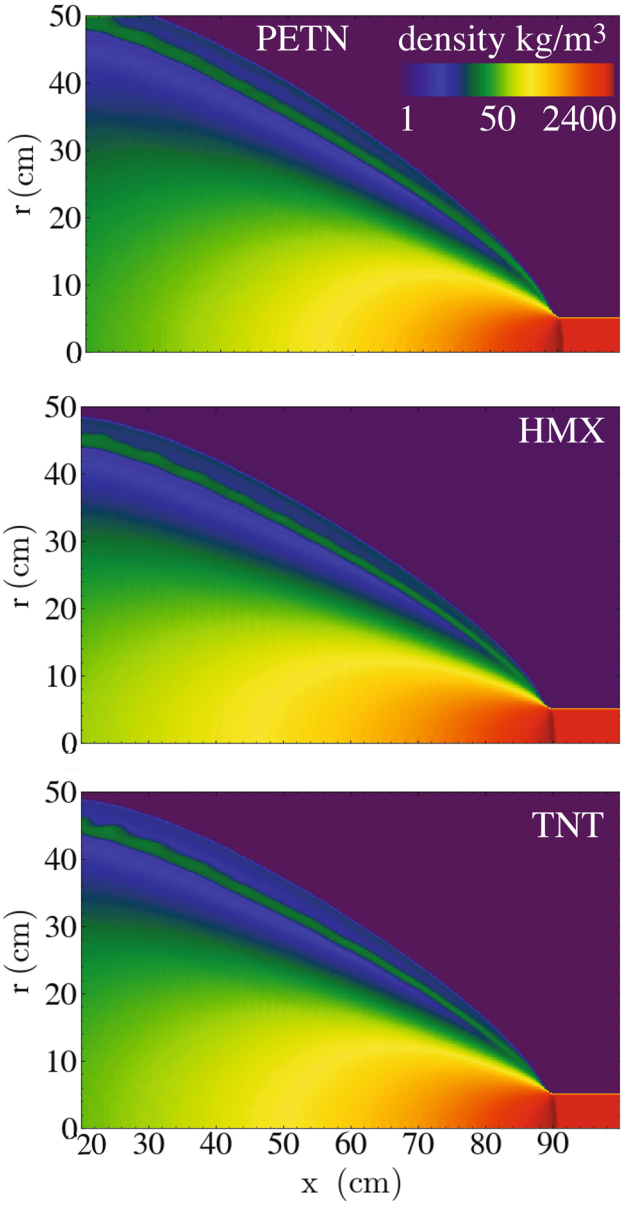

Fig. 20 Effect of explosive material on the detonation and air shock produced by a cylindrical charge for PETN, HMX, and TNT after the detonation propagated a distance of 90 cm. The input parameters to the SBM are $a = 0.75$, $b = 2$, and $p_{\text{ign}} = 2.5$ GPa

tion procedure of the time-based reaction are discussed in Appendix 3.

Figure 21a shows computed results of the ZND structure of a PETN detonation using both the SBM and PB approaches. The detonation for the programmed burn approach was ignited by a plane defined by $x = 0$, which gives $t_{\text{ign}} = x/D_{\text{cj}}$. The computed results show that the ZND structure of the SBM and PB approaches is nearly identical. There are only small differences between the peak pressure in the ZND spike.

Figure 21b shows the shock and detonation structure for a PETN detonation propagating through a cylindrical charge. The PB approach, by design for this numerical experiment, forces the detonation to be perfectly planar. This produces small changes in the shock and expansion structure relative to the reaction model for SBM. Nevertheless, either reaction ignition criterion produces results that are likely acceptable for studying afterburning processes and mid- to far-field air blasts.

10 Summary and conclusions

This paper presented a simplified burn model (SBM) for approximating explosive detonation. Similar to programmed burn approaches, SBM forgoes the accuracy and resolution requirements of traditional reactive burn approaches that can propagate a detonation at the correct wave speed on grid much coarser than the physical width of the reaction zone. The SBM is, instead, focused on scenarios where traditional programmed burn approaches would be of sufficient accuracy. The model is designed to be compatible with

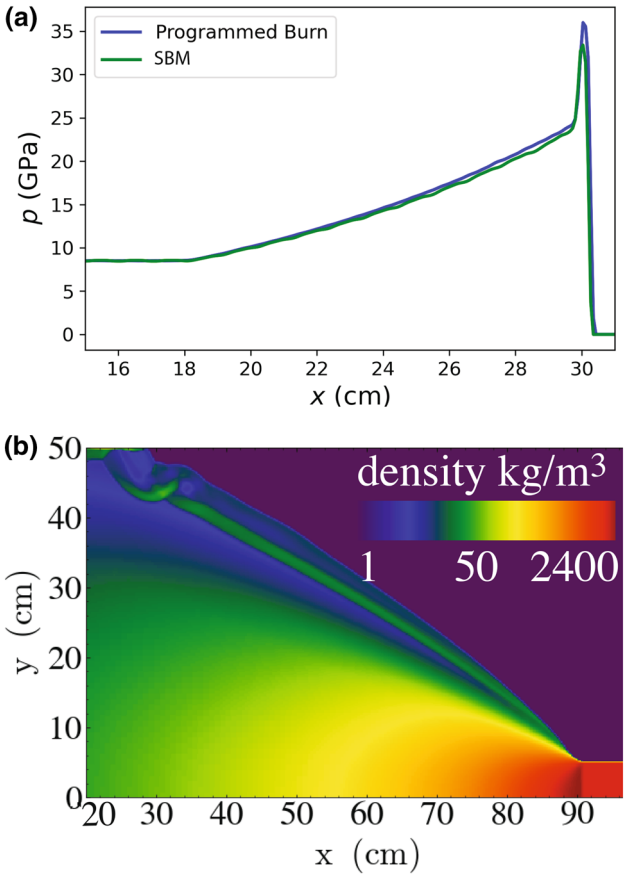

Fig. 21 Computed results of PETN detonations showing **a** a comparison of the ZND structure computed using pressure-based ignition criterion (47) and time-based ignition criterion (57) and **b** shock and detonation structure of a cylindrical charge using the PB model

multiphase reactive flow codes. The SBM is suitable for simulating air blasts, afterburning processes, particle dispersal, and other explosive effects where the fine details of the detonation profile are not important. The model is based on the five-equation multiphase flow equations where homogeneous flow, mechanical equilibrium, and thermal equilibrium are assumed. The governing equations are solved using high-order Godunov shock-capturing techniques.

The SBM uses a simplified reactant equation of state, $p = p_0 + a^2 D_{\text{cj}}^2(\rho - \rho_0)$, where a is a free parameter. This simplified equation of state is based on a linearized pressure–velocity–density relation from the Rankine–Hugoniot jump conditions across an inert shock. The reaction model for the explosive is based on the time it takes a detonation to sweep across a computational cell. This is motivated by detonation burning rules used in traditional programmed burn methods. The reaction model uses a pressure switch to initiate the reaction if the pressure increases above a threshold value. A reaction zone spreading parameter is used in the reaction model to spread the reaction zone over a small number of computational cells, regardless of how coarse the grid is. This spreading parameter prevents unphysical numerical phenomena and instability when the reaction zone is one computational cell or less in width.

The influence of model input parameters on one-dimensional detonations was explored for TNT , PETN, and HMX. Physically realistic CJ detonations with a von Neumann spike are produced if the a is chosen such that the reactant and product Hugoniots do not intersect. Numerical experiments show that selecting $a = 0.75$ is an effective choice that meets this criterion for the explosives explored in this manuscript. The velocity of the detonation was also found to be independent on the pressure threshold and reaction zone spreading parameters for the reaction model. Only the fine details of the detonation structure including the peak pressure in the ZND spike and reaction zone width are influenced by these input parameters. Choosing high values for a produces unphysical weak detonations where the reactant Hugoniot intersects the product Hugoniot prior to the CJ point.

Results on detonations propagating through rate sticks produced similar shock profiles, provided that the input parameters to the reactant EOS and reaction models are in a physically realistic regime. The detonation velocity and fine details of the blast, however, are somewhat dependent on the reaction input parameters. This reaction rate dependence is due to the curvature of multidimensional detonations, which, in turn, is dependent on width of the reaction zone, reaction rate, etc. The pressure-based ignition criterion can be replaced with a time-based ignition criterion using either a burn table from DSD theory or Huygens principle in applications where the curvature effect is undesirable.

Multidimensional numerical experiments show that the blast structure, fireball, and pressure–time traces are relatively independent of the equation of state and reaction model input parameters. The model was also demonstrated to turn corners in complex-shaped explosive charges.

The simplified burn model is effective for simulating the post-detonation processes of explosive detonations. Recommended values for the input parameters a, b, and p_{ign} are 0.75, 2, and 2.5 GPa, respectively. The SBM is relatively straightforward to implement into existing numerical frameworks based on the five-equation multiphase flow model. The SBM also extends straightforwardly to three dimensions. Extensions of this model to incorporate detailed chemical reaction models for afterburning processes and multiphase blasts will be presented in a follow-on paper.

Acknowledgements This work was supported by the United States Air Force Research Laboratory contract number in FA8651-17-F-1033 and United States Air Force Office of Scientific Research Grant Number AFOSR FA9550-19-1-0023. The author would like to thank Brian Taylor for his thoughtful questions and input.

Declarations

Conflict of interest The authors declare that they have no conflict of interest.

Appendix 1 Gas-phase internal energy polynomials

Following Kuhl et al. [10,42], the internal energy for each species is computed using piece-wise second-order polynomials. The internal energy for gas-phase species i is:

$$e_i(T) = a_{i,m} T_g^2 + b_{i,m} T_g + c_{i,m}, \tag{58}$$

where m is an index that corresponds to the temperature interval of the polynomial. The specific heat for gas-phase species i is

$$Cv_i(T) = 2a_{i,m} T_g + b_{i,m}. \tag{59}$$

The thermodynamic data involve five polynomials for each species. The upper and lower temperature boundaries of each polynomial are listed in Table 2. These polynomials are formed based on fits to the Cheetah chemical equilibrium code where the internal energy for each species is computed assuming chemical equilibrium if the temperature is greater than 1800 K and chemically frozen below that value [11]. The polynomial coefficients for each species (DP, AP, and air) are given below.

Temperature is computed from a known e_g using the positive root of the quadratic formula

$$T = \frac{-b_{\text{mix}} + \sqrt{b_{\text{mix}}^2 - 4a_{\text{mix}}\left(c_{\text{mix}} - e_g\right)}}{2a_{\text{mix}}}, \tag{60}$$

where

$$\begin{aligned} a_{\text{mix}} &= \sum Y_i a_{i,m}, \\ b_{\text{mix}} &= \sum Y_i b_{i,m}, \\ c_{\text{mix}} &= \sum Y_i c_{i,m}. \end{aligned} \tag{61}$$

The polynomial interval m is found based on the internal energy of the mixture at the lower and upper temperature bounds of the polynomials. First, we define the internal energy of all species at the boundaries of each polynomial

$$e_{i,m}^{\text{low}} = e_i(T_m^{\text{low}}), \quad e_{i,m}^{\text{high}} = e_i(T_m^{\text{high}}). \tag{62}$$

The polynomial interval, m, is computed from

$$m = j \ \text{ if } \ \sum Y_i e_{i,j}^{\text{low}} \le e_g < \sum Y_i e_{i,j}^{\text{hign}}, \tag{63}$$

where $e_{i,j}^{\text{low}}$ and $e_{i,j}^{\text{hign}}$ are the internal energy for species i evaluated at the lower and upper temperature boundaries for polynomial j.

Table 2 Boundary temperatures for the polynomials

m	1	2	3	4	5
T_m^{low}	300	2340	3700	4150	4530
T_m^{high}	2340	3700	4150	4530	6000

Appendix 1.1 Detonation products, DP

The molecular weight of the detonation products is Mw = 26.9 kg/kmol. The polynomial coefficients for the internal energy polynomials are listed in Tables 3 and 4 for TNT and PETN, respectively.

Appendix 1.2 Afterburning products, AP

The molecular weight of the afterburning products is: Mw = 26.65 kg/kmol. The internal energy polynomial coefficients for TNT and PETN are listed in Tables 5 and 6, respectively.

Appendix 1.3 Air

The molecular weight of air is Mw = 28.85 kg/kmol. The internal energy polynomial coefficients are listed in Table 7.

Table 3 Polynomial coefficients for TNT detonation products in units of cal/g [42]

m	a	b	c
1	5.3244e−5	0.17393	−941.33
2	7.9903e−5	0.035886	−760.12
3	0.0000	1.80555	−6211.8
4	4.5108e−4	−2.7713	5014.0
5	2.578e−3	−22.917	52697.0

Table 4 Polynomial coefficients for PETN detonation products in units of cal/g [42]

m	a	b	c
1	3.31674e−5	0.20867	−1890.164
2	5.97088e−5	0.03770	−1634.868
3	1.9052e−4	−0.89226	20.04935
4	2.28177e−4	−1.20053	651.0422
5	1.78281e−4	−0.774255	−248.616

Table 5 Polynomial coefficients for TNT-air afterburning products in units of cal/g [42]

m	a	b	c
1	3.5282e−6	0.25361	−949.3
2	2.5302e−4	−0.80169	168.08
3	−6.1238e−5	1.5345	−4178
4	−3.9217e−4	4.2413	−9713.6
5	2.7654e−5	0.2432	−195.0

Table 6 Polynomial coefficients for PETN-air afterburning products in units of cal/g [42]

m	a	b	c
1	4.745e−5	0.1549	−1555.6
2	4.6038e−4	−1.7722	711.74
3	4.9083e−4	−1.841	558.87
4	−6.1549e−4	7.3463	−18515.0
5	−2.8216e−4	3.8022	−9254.5

Table 7 Polynomial coefficients for air in units of cal/g [42]

m	a	b	c
1	2.02768e−5	0.16498	−71.9172
2	1.34322e−4	−0.41045	658.24424
3	7.01281e−5	0.11507	−403.36139
4	−1.02084e−4	1.53731	−3340.674
5	4.04923e−5	0.11381	148.38643

Appendix 2 Jacobian entries for mixed cell P–T equilibration

The Jacobian entries for pressure–temperature equilibration in (40) are

$$J_{1,1} = \alpha_g \frac{\partial \rho_g}{\partial p} + \alpha_h \frac{\partial \rho_h}{\partial p} \tag{64}$$

$$J_{1,2} = \alpha_g \frac{\partial \rho_g}{\partial T} \tag{65}$$

$$J_{2,1} = \alpha_g \left(e_g \frac{\partial \rho_g}{\partial p} + \rho_g \frac{\partial e_g}{\partial p} \right) + \alpha_h \left(e_h \frac{\partial \rho_h}{\partial p} + \rho_h \frac{\partial e_h}{\partial p} \right) \tag{66}$$

$$J_{2,2} = \alpha_g \left(e_g \frac{\partial \rho_g}{\partial T} + \rho_g \frac{\partial e_h}{\partial T} \right) + \alpha_h \left(e_h \frac{\partial \rho_h}{\partial T} + \rho_h \frac{\partial e_h}{\partial T} \right). \tag{67}$$

The thermodynamic derivatives needed for the Jacobian are

$$\left. \frac{\partial \rho_g}{\partial p} \right|_T = \frac{1}{c_n^2 + R_{\text{mix}} T} \tag{68}$$

$$\left. \frac{\partial \rho_g}{\partial T} \right|_p = -\frac{R_{\text{mix}} \rho_g}{c_n^2 + R_{\text{mix}} T} \tag{69}$$

$$\left. \frac{\partial e_g}{\partial T} \right|_p = C v_g \tag{70}$$

$$\left. \frac{\partial e_g}{\partial p} \right|_T = 0 \tag{71}$$

for the gas-phase JWL EOS and

$$\left. \frac{\partial \rho_h}{\partial p} \right|_T = \frac{1}{\left(a D_{\text{cj}} \right)^2} \tag{72}$$

$$\left. \frac{\partial e_h}{\partial T} \right|_p = C v_h \tag{73}$$

$$\left. \frac{\partial e_h}{\partial p} \right|_T = \left. \frac{\partial e_h}{\partial \rho_h} \right|_T \left. \frac{\partial \rho_h}{\partial p} \right|_T = \frac{p}{\left(\rho_h a D_{\text{cj}} \right)^2} \tag{74}$$

for the solid-phase EOS.

Appendix 3 Numerical methods

The governing equations can be written as

$$\frac{\partial \mathbf{U}}{\partial t} + \frac{\partial \mathbf{F}}{\partial x} + \frac{\partial \mathbf{G}}{\partial y} + \eta \frac{\mathbf{F}}{x} + \mathbf{I} = \mathbf{S}, \tag{75}$$

where

$$\mathbf{U} = \begin{bmatrix} \alpha_h \\ \alpha_h \rho_h \\ \alpha_g \rho_g Y_{g,1} \\ \vdots \\ \alpha_g \rho_g Y_{g,N} \\ \rho u \\ \rho v \\ \rho E \end{bmatrix}, \quad \mathbf{S} = \begin{bmatrix} -\dot{M}/\rho_h \\ -\dot{M} \\ Y_{cj,1} \dot{M} + \dot{\omega}_{g,1} \\ \vdots \\ Y_{cj,N} \dot{M} + \dot{\omega}_{g,N} \\ 0 \\ 0 \\ 0 \end{bmatrix}, \tag{76}$$

$$\mathbf{F} = \begin{bmatrix} \alpha_h u \\ \alpha_h \rho_h u \\ \alpha_g \rho_g u Y_{g,1} \\ \vdots \\ \alpha_g \rho_g u Y_{g,N} \\ \rho u u \\ \rho v u \\ \rho H u \end{bmatrix}, \quad \mathbf{G} = \begin{bmatrix} \alpha_h v \\ \alpha_h \rho_h v \\ \alpha_g \rho_g v Y_{g,1} \\ \vdots \\ \alpha_g \rho_g v Y_{g,N} \\ \rho u v \\ \rho v v \\ \rho H v \end{bmatrix}, \tag{77}$$

$$\mathbf{I} = \begin{bmatrix} -\alpha_{\mathrm{h}} \left(\frac{\partial \hat{u}}{\partial x} + \frac{\partial \hat{v}}{\partial y} + \eta \frac{u}{x} \right) \\ 0 \\ 0 \\ \vdots \\ 0 \\ \frac{\partial p}{\partial x} \\ \frac{\partial p}{\partial y} \\ 0 \end{bmatrix}, \tag{78}$$

and η is an axisymmetric coordinate system selector in two dimensions. ($\eta = 0$ for Cartesian coordinates and $\eta = 1$ for axisymmetric coordinates.)

An operator splitting method is used to solve the governing equations [65]. The conserved variable vector, $\mathbf{U}$, is advanced from time t to $t + 2\Delta t$ by

$$\mathbf{U}^{t+2\Delta t} = \mathcal{H}^{\Delta t} \left(\mathcal{S}^{2\Delta t} \left(\mathcal{H}^{\Delta t} (\mathbf{U}^{t}) \right) \right) \tag{79}$$

where $\mathcal{H}^{\Delta t}$ represents integration of the hyperbolic terms for a time step of Δt and $\mathcal{S}^{2\Delta t}$ represent integration of the chemical source terms for a time-step size of $2\Delta t$. The solution procedure for the hyperbolic and source term operators is discussed in turn.

Appendix 3.1 Hyperbolic operator, $\mathcal{H}^{\Delta t}$

The method of lines is used to advance the hyperbolic operator, $\mathcal{H}^{\Delta t}$. A high-order Godunov approach [51] is used to approximate the spatial derivatives

$$\frac{\partial \psi}{\partial x} \approx \frac{\psi_{i+\frac{1}{2},j} - \psi_{i-\frac{1}{2},j}}{\Delta x}, \frac{\partial \psi}{\partial y} \approx \frac{\psi_{i,j+\frac{1}{2}} - \psi_{i,j-\frac{1}{2}}}{\Delta y}, \tag{80}$$

where the values of fluxes at the computational cell edges are computed using an approximate Riemann solver [54–56]. The resulting ordinary differential equations at each computational cell are time-marched using strong stability preserving Runge–Kutta [57].

The primitive variable $(\alpha_{\mathrm{h}}, p, T, u, v, Y_i)$ are reconstructed to each cell edge using a fifth-order MUSCL approach [51,52]

$$\begin{aligned} \tilde{\psi}^{\mathrm{L}}_{i+\frac{1}{2},j} = \frac{1}{60} [& 2\psi_{i-2,j} - 13\psi_{i-1,j} \\ & + 47\psi_{i,j} + 27\psi_{i+1,j} - 3\psi_{i+2,j}] \end{aligned} \tag{81}$$

A TVD limiter is used to enforce monotonicity of $\psi^{\mathrm{L}}_{i+\frac{1}{2},j}$ [52,53]

$$\psi^{\mathrm{L}}_{i+\frac{1}{2},j} = \psi_{i,j} + \frac{1}{2} \phi \left(\psi_{i,j} - \psi_{i-1,j} \right), \tag{82}$$

where

$$\phi = \max \left[0, \min \left(2, 2 \frac{\psi_{i+1,j} - \psi_{i,j}}{\psi_{i,j} - \psi_{i-1,j}}, 2 \frac{\tilde{\psi}^{\mathrm{L}}_{i+\frac{1}{2},j} - \psi_{i,j}}{\psi_{i,j} - \psi_{i-1,j}} \right) \right]. \tag{83}$$

Stencil symmetry is used to compute the right-biased interpolation $\psi^{\mathrm{R}}_{i+\frac{1}{2},j}$.

The HLLCM approximate Riemann solver is used to compute the numerical fluxes from the edge values [56]. The HLLCM flux completely avoids carbuncle instabilities and other numerical shock anomalies. The left and right interpolated variables are used to compute the flux vector ($\mathbf{F}$ and $\mathbf{G}$), pressure, and advection velocity ($\hat{u}$ and $\hat{v}$) at computational cell edges by:

$$\mathbf{F}_{i+\frac{1}{2},j} = \begin{cases} \mathbf{F}^{\mathrm{L}} & \text{if } 0 \le S^{\mathrm{L}} \\ \mathbf{F}^{\mathrm{L}*} & \text{if } S^{\mathrm{L}} \le 0 \le S^{*} \\ \mathbf{F}^{\mathrm{R}*} & \text{if } S^{*} \le 0 \le S^{\mathrm{R}} \\ \mathbf{F}^{\mathrm{R}} & \text{if } S^{\mathrm{R}} \le 0, \end{cases} \tag{84}$$

where

$$\boldsymbol{F}^{\mathrm{K}} = \begin{bmatrix} \alpha^{\mathrm{K}}_{\mathrm{h}} u^{\mathrm{K}} \\ \alpha^{\mathrm{K}}_{\mathrm{h}} \rho^{\mathrm{K}}_{\mathrm{h}} u^{\mathrm{K}} \\ \alpha^{\mathrm{K}}_{\mathrm{g}} \rho^{\mathrm{K}}_{\mathrm{g}} u^{\mathrm{K}} \\ \alpha^{\mathrm{K}}_{\mathrm{g}} \rho^{\mathrm{K}}_{\mathrm{g}} u^{\mathrm{K}} Y^{\mathrm{K}}_{\mathrm{g},i} \\ \rho^{\mathrm{K}} u^{\mathrm{K}} u^{\mathrm{K}} \\ \rho^{\mathrm{K}} u^{\mathrm{K}} v^{\mathrm{K}} \\ \rho^{\mathrm{K}} u^{\mathrm{K}} H^{\mathrm{K}} \end{bmatrix}, \tag{85}$$

$$\boldsymbol{F}^{\mathrm{K}*} = \begin{bmatrix} \alpha^{\mathrm{K}*}_{\mathrm{h}} S^{*} \\ \alpha^{\mathrm{K}}_{\mathrm{h}} \rho^{\mathrm{K}*}_{\mathrm{h}} S^{*} \\ \alpha^{\mathrm{K}}_{\mathrm{g}} \rho^{\mathrm{K}*}_{\mathrm{g}} S^{*} \\ \alpha^{\mathrm{K}}_{\mathrm{g}} \rho^{\mathrm{K}*}_{\mathrm{g}} S^{*} Y_{\mathrm{g},i} \\ \rho^{\mathrm{K}*} S^{*} S^{*} \\ \rho^{\mathrm{K}*} S^{*} v^{\mathrm{K}*} + (1-f) O^{*}_{\mathrm{HLL}} \\ \rho^{\mathrm{K}*} S^{*} E^{\mathrm{K}*} + p^{*} S^{*} + \frac{1}{2}(1-f) Q^{\mathrm{K}*} \end{bmatrix}, \tag{86}$$

the superscript K refers to either the L or R states based on the interpolated variables. The pressure used to compute the pressure gradient is given by:

$$p_{i+1/2,j} = \begin{cases} p^{\mathrm{L}} & \text{if } 0 \le S^{\mathrm{L}} \\ p^{\mathrm{R}} & \text{if } S^{\mathrm{R}} \le 0, \\ p^{*} & \text{otherwise.} \end{cases} \tag{87}$$

The density, volume fraction, and total energy in the middle states are:

$$\rho_{\mathrm{h}}^{\mathrm{K}*} = \rho_{\mathrm{h}}^{\mathrm{K}} \frac{S^{\mathrm{K}} - u^{\mathrm{K}}}{S^{\mathrm{K}} - S^*}, \tag{88}$$

$$\rho_{\mathrm{g}}^{\mathrm{K}*} = \rho_{\mathrm{g}}^{\mathrm{K}} \frac{S^{\mathrm{K}} - u^{\mathrm{K}}}{S^{\mathrm{K}} - S^*}, \tag{89}$$

$$\rho^{\mathrm{K}*} = \rho^{\mathrm{K}} \frac{S^{\mathrm{K}} - u^{\mathrm{K}}}{S^{\mathrm{K}} - S^*}, \tag{90}$$

$$\alpha_{\mathrm{h}}^{\mathrm{K}*} = \alpha_{\mathrm{h}}^{\mathrm{K}} \frac{S^{\mathrm{K}} - u^{\mathrm{K}}}{S^{\mathrm{K}} - S^*}. \tag{91}$$

The wave speeds, S^{L} and S^{R}, are estimated using Davis's method [65]

$$\begin{aligned} S^{\mathrm{L}} &= \min(u^{\mathrm{L}} - c^{\mathrm{L}}, u^{\mathrm{R}} - c^{\mathrm{R}}) \\ S^{\mathrm{R}} &= \min(u^{\mathrm{R}} + c^{\mathrm{R}}, u^{\mathrm{R}} + c^{\mathrm{R}}). \end{aligned} \tag{92}$$

Then, the velocity of the contact surface (S^*) is

$$S^* = \frac{p_{\mathrm{g}}^{\mathrm{R}} - p_{\mathrm{g}}^{\mathrm{L}} + \beta^{\mathrm{L}} u^{\mathrm{L}} - \beta^{\mathrm{R}} u^{\mathrm{R}}}{\beta^{\mathrm{L}} - \beta^{\mathrm{R}}}, \tag{93}$$

and the pressure in the middle state is

$$p^* = p^{\mathrm{L}} + \rho^{\mathrm{L}}(S^{\mathrm{L}} - u^{\mathrm{L}})(S^* - u^{\mathrm{L}}), \tag{94}$$

where

$$\begin{aligned} \beta^{\mathrm{L}} &= \rho^{\mathrm{L}} \left(S^{\mathrm{L}} - u^{\mathrm{L}}\right), \\ \beta^{\mathrm{R}} &= \rho^{\mathrm{R}} \left(S^{\mathrm{R}} - u^{\mathrm{R}}\right). \end{aligned} \tag{95}$$

The middle-state total energies are:

$$E^{\mathrm{K}*} = E^{\mathrm{K}} + \left(S^* - u^{\mathrm{K}}\right)\left(S^* + \frac{p^{\mathrm{K}}}{\beta^{\mathrm{K}}}\right) \tag{96}$$

The parameters $v^{\mathrm{K}*}$, O^*_{HLL}, and $Q^{\mathrm{K}*}$ add dissipation in the shear wave near shocks to avoid the carbuncle instability near strong grid-aligned shocks

$$v^{\mathrm{K}*} = f v^{\mathrm{K}} + (1 - f)\frac{\beta^{\mathrm{R}} v^{\mathrm{R}} - \beta^{\mathrm{L}} v^{\mathrm{L}}}{\beta^{\mathrm{R}} - \beta^{\mathrm{L}}}, \tag{97}$$

$$O^*_{\mathrm{HLL}} = -\frac{\beta^{\mathrm{L}}\beta^{\mathrm{R}}(v^{\mathrm{L}} - v^{\mathrm{R}})}{\beta^{\mathrm{R}} - \beta^{\mathrm{L}}}, \tag{98}$$

$$\begin{aligned} Q^{\mathrm{K}*} = \rho^{\mathrm{K}*} S^* &\left[\frac{\beta^{\mathrm{R}}(v^{\mathrm{R}})^2 - \beta^{\mathrm{L}}(v^{\mathrm{L}})^2}{\beta^{\mathrm{R}} - \beta^{\mathrm{L}}} - (v^{\mathrm{K}})^2\right] \\ &+ \frac{\beta^{\mathrm{L}}\beta^{\mathrm{R}}\left[(v^{\mathrm{R}})^2 - (v^{\mathrm{L}})^2\right]}{\beta^{\mathrm{R}} - \beta^{\mathrm{L}}}, \end{aligned} \tag{99}$$

where f is a shock sensor [56]

$$f = \begin{cases} 1, & \text{if } \max\left(\Delta p_{i-1:i+2,j}\right) > p_r \\ 0, & \text{else} \end{cases} \tag{100}$$

and

$$\begin{aligned} \Delta p_{i,j} = \max\Big(&|p_{i+1,j} - p_{i,j}|, |p_{i-1,j} - p_{i,j}|, \\ &|p_{i,j+1} - p_{i,j}|, |p_{i,j-1} - p_{i,j}|\Big)/p_{i,j}. \end{aligned} \tag{101}$$

The fractional pressure rise for the shock sensor is $p_r = 0.1$.

The non-conservative term in the volume fraction advection equation, $\alpha_{\mathrm{h}}\nabla\cdot\mathbf{v}$, is approximated by [37,38]

$$\begin{aligned} \alpha_{\mathrm{h}}\nabla\cdot\mathbf{v} \approx \alpha_{\mathrm{h},i,j}\Bigg[&\frac{\hat{u}_{i+\frac{1}{2},j} - \hat{u}_{i+\frac{1}{2},j}}{\Delta x} \\ &+ \frac{\hat{v}_{i,j+\frac{1}{2}} - \hat{v}_{i,j+\frac{1}{2}}}{\Delta y} + \eta\frac{u_{i,j}}{x}\Bigg], \end{aligned} \tag{102}$$

where

$$\hat{u}_{i+\frac{1}{2},j} = \begin{cases} u^{\mathrm{L}} & \text{if } 0 \le S^{\mathrm{L}} \\ S^*\frac{S^{\mathrm{L}} - u^{\mathrm{L}}}{S^{\mathrm{L}} - S^*} & \text{if } S^{\mathrm{L}} \le 0 \le S^* \\ S^*\frac{S^{\mathrm{R}} - u^{\mathrm{R}}}{S^{\mathrm{R}} - S^*} & \text{if } S^* \le 0 \le S^{\mathrm{R}} \\ u^{\mathrm{R}} & \text{if } S^{\mathrm{R}} \le 0. \end{cases} \tag{103}$$

The edge values of the flux vector, pressure, and volume fraction advection velocity on the y- (and z-) directions of the computational cells are computed on a directional basis. The governing equations and solution method extend to straightforwardly to three dimensions.

Appendix 3.2 Source term operator, $\mathcal{S}^{2\Delta t}$

The reaction term for the detonation mass rate of consumption, $\dot{M}$, and gas-phase homogeneous reactions, $\dot{\omega}_{\mathrm{g},i}$, are computed sequentially. First, the detonation reaction is integrated. Then, the homogeneous afterburning reactions are integrated in a separate step.

Appendix 3.2.1 Integration of the detonation reaction

The differential equations for the detonation reaction source terms are:

$$\frac{\mathrm{d}\alpha_{\mathrm{h}}}{\mathrm{d}t} = -\dot{\alpha} \tag{104}$$

$$\frac{\mathrm{d}\alpha_{\mathrm{h}}\rho_{\mathrm{h}}}{\mathrm{d}t} = -\dot{\alpha}\rho_{\mathrm{h}} \tag{105}$$

$$\frac{\mathrm{d}\alpha_{\mathrm{g}}\rho_{\mathrm{g}}Y_{\mathrm{g},i}}{\mathrm{d}t} = Y_{\mathrm{cj},i}\dot{\alpha}\rho_{\mathrm{h}}. \tag{106}$$

The change in explosive volume $\delta\alpha_\mathrm{h}$ can be defined by integrating the volume fraction equation and using the definition that $\dot{\alpha}$ is constant

$$\delta\alpha = \min\left(\alpha_\mathrm{h}^t, \delta t\dot{\alpha}\right), \tag{107}$$

where

$$\delta t = \begin{cases} 2\Delta t \ \ \text{SBM} \\ \max(0, \min(t + 2\Delta t - t_\mathrm{ign}, \Delta t)) \ \ \text{PB model} \end{cases} \tag{108}$$

Then,

$$(\alpha_\mathrm{h})^{t+2\Delta t} = (\alpha_\mathrm{h})^t - \delta\alpha \tag{109}$$

$$(\alpha_\mathrm{h}\rho_\mathrm{h})^{t+2\Delta t} = (\alpha_\mathrm{h}\rho_\mathrm{h})^t - \rho_\mathrm{h}\delta\alpha \tag{110}$$

$$(\alpha_\mathrm{g}\rho_\mathrm{g}Y_{\mathrm{g},i})^{t+2\Delta t} = (\alpha_\mathrm{g}\rho_\mathrm{g}Y_{\mathrm{g},i})^t + Y_{\mathrm{cj},i}\rho_\mathrm{h}\delta\alpha. \tag{111}$$

During numerical integration, it is possible that explosive mass and volume fraction can become slightly desynchronized. If $\alpha_\mathrm{h} = 0$, but $\alpha_\mathrm{h}\rho_\mathrm{h} > 0$, the extra explosive mass is converted to gas-phase products. If $\alpha_\mathrm{h}\rho_\mathrm{h} = 0$, but $\alpha_\mathrm{h} > 0$ the explosive volume fraction is set to zero without any mass exchange.

Appendix 3.3 Integration of homogeneous reactions

The differential equations describing the homogeneous reaction process are:

$$\frac{\mathrm{d}\alpha_\mathrm{g}\rho_\mathrm{g}Y_{\mathrm{g},i}}{\mathrm{d}t} = \alpha_\mathrm{h}\dot{\omega}_i. \tag{112}$$

This formulation is applicable to reactions with arbitrary complexity. However, the afterburning of fuel-rich detonation products is assumed to be infinite rate and mixing-limited. The global reaction proceeds in a single-step irreversible reaction on a mass basis:

$$\mathrm{DP} + \nu\mathrm{Air} \rightarrow (1 + \nu)\mathrm{AP}, \tag{113}$$

where ν is the stoichiometric fuel–air ratio between the detonation products (DP) and air. The afterburning reaction is assumed to proceed at an infinite reaction rate.

The gas-phase afterburning step is implemented as:

$$\alpha_\mathrm{g}\rho_\mathrm{g}\frac{\mathrm{d}Y_{\mathrm{g},i}}{\mathrm{d}t} = \alpha_\mathrm{g}\dot{\omega}_i, \tag{114}$$

where $\dot{\omega}_i$ is the mass rate of production for species i. The afterburning reaction is assumed to progress infinitely fast. Thus, any fuel and air in a computational cell is burned instantly to produce products and leftover fuel or air. These infinite rate reactions are integrated by defining the change of product mass fraction based on the deficient reactant

$$\delta Y_\mathrm{AP} = \min\left[Y_\mathrm{DP}^t(1 + \nu), Y_\mathrm{Air}^t\frac{1 + \nu}{\nu}\right]. \tag{115}$$

Then, the updated mass fractions are:

$$Y_\mathrm{DP}^{t+2\Delta t} = Y_\mathrm{DP}^t - \delta Y_\mathrm{AP}\frac{1}{1 + \nu}, \tag{116}$$

$$Y_\mathrm{Air}^{t+2\Delta t} = Y_\mathrm{Air}^t - \delta Y_\mathrm{AP}\frac{\nu}{1 + \nu}, \tag{117}$$

$$Y_\mathrm{AP}^{t+2\Delta t} = Y_\mathrm{AP}^t + \delta Y_\mathrm{AP}, \tag{118}$$

where Y_DP^t, Y_Air^t, Y_AP^t are the initial values of the gas-phase detonation product, air, and afterburning product mass fractions, respectively, at time t. Finally, the gas-phase species mass is updated as:

$$\left(\alpha_\mathrm{g}\rho_\mathrm{g}Y_{\mathrm{g},i}\right)^{t+2\delta t} = \left(\alpha_\mathrm{g}\rho_\mathrm{g}\right)^t Y_{\mathrm{g},i}^{t+2\Delta t}. \tag{119}$$

References

1. Frost, D.L., Gregoire, Y., Patel, O., Goroshin, S., Zhang, F.: Particle jet formation during explosive dispersal of solid particles. Phys. Fluids **24**, 091109 (2012). https://doi.org/10.1063/1.4751876
2. Frost, D.: Heterogeneous/particle-laden blast waves. Shock Waves **28**, 439–449 (2018). https://doi.org/10.1007/s00193-018-0825-1
3. Koneru, R.B., Rollin, B., Durant, B., Ouellet, F., Balachandar, S.: A numerical study of particle jetting in a dense particle bed driven by an air-blast. Phys. Fluids **32**(9), 093301 (2020). https://doi.org/10.1063/5.0015190
4. Sugiyama, Y., Homae, T., Matsumura, T., Wakabayashi, K.: Numerical study on the attenuation effect on the blast wave of encircling a high explosive with granular media. J. Appl. Phys. **127**(16), 164701 (2020). https://doi.org/10.1063/1.5143351
5. Fedina, E., Gottiparthi, K.C., Fureby, C., Menon, S.: Combustion in afterburning behind explosive blasts. In: Grinstein, F.F. (ed.) Coarse Grained Simulation and Turbulent Mixing, pp. 393–431. Cambridge University Press, Cambridge (2016). https://doi.org/10.1017/CBO9781316480243.015
6. McNesby, K., Homan, B., Ritter, J., Quine, Z., Ehlers, R., McAndrew, B.: Afterburn ignition delay and shock augmentation in fuel rich solid explosives. Propellants Explos. Pyrotech. **35**(1), 57–65 (2010). https://doi.org/10.1002/prep.200800084
7. Donahue, L., Zhang, F., Ripley, R.: Numerical models for afterburning of TNT detonation products in air. Shock Waves **23**(6), 559–573 (2013). https://doi.org/10.1007/s00193-013-0467-2
8. Edri, I., Feldgun, V., Karinski, Y., Yankelevsky, D.: Afterburning aspects in an internal TNT explosion. Int. J. Prot. Struct. **4**(1), 97–116 (2013). https://doi.org/10.1260/2041-4196.4.1.97
9. Kim, C.K., Lai, M.C., Zhang, Z.C., Cook, G., Im, K.S.: Modeling and numerical simulation of afterburning of thermobaric explosives in a closed chamber. Int. J. Precis. Eng. Manuf. **18**(7), 979–986 (2017). https://doi.org/10.1007/s12541-017-0115-3
10. Kuhl, A., Bell, J., Beckner, V.: Heterogeneous continuum model of aluminum particle combustion in explosions. Combust. Explos. Shock Waves **46**(4), 433–448 (2010). https://doi.org/10.1007/s10573-010-0058-9

11. Kuhl, A.L., Bell, J.B., Beckner, V.E., Balakrishnan, K., Aspden, A.J.: Spherical combustion clouds in explosions. Shock Waves **23**(3), 233–249 (2013). https://doi.org/10.1007/s00193-012-0410-y
12. Posey, J., Roque, B., Guhathakurta, S., Houim, R.W.: Mechanisms of prompt and delayed ignition and combustion of explosively-dispersed aluminum powder. Phys. Fluids **33**, 113308 (2021). https://doi.org/10.1063/5.0065312
13. Bdzil, J.B., Stewart, D.S.: The dynamics of detonation in explosive systems. Annu. Rev. Fluid Mech. **39**(1), 263–292 (2007). https://doi.org/10.1146/annurev.fluid.38.050304.092049
14. Hernández, A.M., Stewart, D.S.: Computational modelling of multi-material energetic materials and systems. Combust. Theory Model. **24**(3), 407–441 (2020). https://doi.org/10.1080/13647830.2019.1689299
15. Kapila, A., Bdzil, J.B., Stewart, D.S.: On the structure and accuracy of programmed burn. Combust. Theory Model. **10**(2), 289–321 (2006). https://doi.org/10.1080/13647830500436540
16. Fickett, W., Davis, W.C.: Detonation: Theory and Experiment. Dover, Mineola (2000)
17. Jackson, T.L., Zhang, J., Short, M.: Multiscale approach to shock to detonation transition in energetic materials. Propellants Explos. Pyrotech. **45**(2), 316–329 (2020). https://doi.org/10.1002/prep.201900179
18. Hill, L.G.: Is the detonation "dead zone" really dead? Proc. Combust. Inst. **35**(2), 2041–2049 (2015). https://doi.org/10.1016/j.proci.2014.10.001
19. Menikoff, R.: Accuracy of high explosive data used for reactive burn model calibration. Technical Report, Los Alamos National Lab. (LANL), Los Alamos, NM (United States) (2020)
20. Garno, J., Ouellet, F., Bae, S., Jackson, T.L., Kim, N.H., Haftka, R., Hughes, K.T., Balachandar, S.: Calibration of reactive burn and Jones–Wilkins–Lee parameters for simulations of a detonation-driven flow experiment with uncertainty quantification. Phys. Rev. Fluids **5**, 123201 (2020). https://doi.org/10.1103/PhysRevFluids.5.123201
21. Aslam, T.D., Price, M.A., Ticknor, C., Coe, J.D., Leiding, J.A., Zocher, M.A.: AWSD calibration for the HMX based explosive PBX 9501. AIP Conf. Proc. **2272**(1), 030001 (2020). https://doi.org/10.1063/12.0000891
22. Bdzil, J., Stewart, D., Jackson, T.: Program burn algorithms based on detonation shock dynamics: discrete approximations of detonation flows with discontinuous front models. J. Comput. Phys. **174**(2), 870–902 (2001). https://doi.org/10.1006/jcph.2001.6942
23. Bdzil, J.B., Stewart, D.S.: Theory of detonation shock dynamics. In: Zhang, F. (ed.) Shock Waves Science and Technology Library, Vol. 6: Detonation Dynamics, pp. 373–453. Springer, Berlin (2012). https://doi.org/10.1007/978-3-642-22967-1_7
24. Kenamond, M.: Lund high explosive programmed burn model in the flag code. User and Developer Documentation. LANL. LA-UR-09-08297 (2009)
25. Mandell, D., Burton, D., Lund, C.: High explosive programmed burn in the flag code. Technical Report, Los Alamos National Lab., NM (United States) (1998)
26. Türker, L.: Thermobaric and enhanced blast explosives (EBX). Defence Technol. **12**(6), 423–445 (2016)
27. Williams, P.T.: A simple reactive-flow model for corner-turning in insensitive high explosives, including failure and dead zones. I. The model. Propellants Explos. Pyrotech. **45**(10), 1506–1522 (2020). https://doi.org/10.1002/prep.201900383
28. Kapila, A.K., Menikoff, R., Bdzil, J.B., Son, S.F., Stewart, D.S.: Two-phase modeling of deflagration-to-detonation transition in granular materials: reduced equations. Phys. Fluids **13**(10), 3002–3024 (2001). https://doi.org/10.1063/1.1398042
29. Allaire, G., Clerc, S., Kokh, S.: A five-equation model for the simulation of interfaces between compressible fluids. J. Comput. Phys. **181**(2), 577–616 (2002). https://doi.org/10.1006/jcph.2002.7143
30. Baer, M.R., Nunziato, J.W.: A two-phase mixture theory for the deflagration-to-detonation transition (DDT) in reactive granular materials. Int. J. Multiph. Flow **12**(6), 861–889 (1986). https://doi.org/10.1016/0301-9322(86)90033-9
31. Schmitt, R.G.: Toward a new paradigm for reactive flow modeling. AIP Conf. Proc. **845**(1), 1109–1112 (2006). https://doi.org/10.1063/1.2263517
32. Saurel, R., Abgrall, R.: A multiphase Godunov method for compressible multifluid and multiphase flows. J. Comput. Phys. **150**(2), 425–467 (1999). https://doi.org/10.1006/jcph.1999.6187
33. Schwendeman, D.W., Wahle, C.W., Kapila, A.K.: The Riemann problem and a high-resolution Godunov method for a model of compressible two-phase flow. J. Comput. Phys. **212**(2), 490–526 (2006). https://doi.org/10.1016/j.jcp.2005.07.012
34. Schwendeman, D., Kapila, A., Henshaw, W.: A study of detonation diffraction and failure for a model of compressible two-phase reactive flow. Combust. Theory Model. **14**(3), 331–366 (2010). https://doi.org/10.1080/13647830.2010.489955
35. Bdzil, J.B., Kapila, A.K., Hennessey, M.P.: Shock structure for the seven-equation, two-phase continuum-mixture model. Combust. Theory Model. (2021). https://doi.org/10.1080/13647830.2021.1889683
36. Houim, R.W., Oran, E.S.: A multiphase model for compressible granular-gaseous flows: formulation and initial tests. J. Fluid Mech. **789**, 166–220 (2016). https://doi.org/10.1017/jfm.2015.728
37. Johnsen, E., Colonius, T.: Implementation of WENO schemes in compressible multicomponent flow problems. J. Comput. Phys. **219**(2), 715–732 (2006). https://doi.org/10.1016/j.jcp.2006.04.018
38. Coralic, V., Colonius, T.: Finite-volume WENO scheme for viscous compressible multicomponent flows. J. Comput. Phys. **274**, 95–121 (2014). https://doi.org/10.1016/j.jcp.2014.06.003
39. Zukas, J.A., Walters, W., Walters, W.P.: Explosive Effects and Applications. Springer, Berlin (2002)
40. Wescott, B.L., Stewart, D.S., Davis, W.C.: Equation of state and reaction rate for condensed-phase explosives. J. Appl. Phys. **98**(5), 053514 (2005). https://doi.org/10.1063/1.2035310
41. Fried, L.E., Clark Souers, P.: BKWC: an empirical BKW parametrization based on cylinder test data. Propellants Explos. Pyrotech. **21**(4), 215–223 (1996). https://doi.org/10.1002/prep.19960210411
42. Kuhl, A.L., Khasainov, B.: Quadratic model of thermodynamic states in SDF explosions. 37th International Annual Conference of Energetic Materials Characterisation and Performance of Advanced Systems, pp. 143.1–143.11. Karlsruhe, Germany (2007)
43. Callen, H.B.: Thermodynamics and Introduction to Thermostatistics. Wiley, New York (1985)
44. Poling, B.E., Prausnitz, J.M., O'Connel, J.P.: The Properties of Gases and Liquids, 5th edn. McGraw Hill, New York (2001)
45. Lee, K., Hernández, A.M., Stewart, D.S.: Well-posed equations of states for condensed-phase explosives. Propellants Explos. Pyrotech. **45**(3), 374–386 (2020). https://doi.org/10.1002/prep.201900121
46. Short, M., Chiquete, C., Bdzil, J.B., Quirk, J.J.: Detonation diffraction in a circular arc geometry of the insensitive high explosive PBX 9502. Combust. Flame **196**, 129–143 (2018). https://doi.org/10.1016/j.combustflame.2018.06.002
47. Stewart, D.S., Yoo, S., Davis, W.C.: Equation of state for modeling the detonation reaction zone. 12th Symp. (Intl) on Detonation, pp. 1–11 (2002)
48. Tarver, C.M., Hallquist, J.O., Erickson, L.M.: Modeling short pulse duration shock initiation of solid explosives. 8th International Symposium on Detonation. Albuquerque, New Mexico (1985)

49. LeVeque, R.J.: Finite Volume Methods for Hyperbolic Problems. Cambridge University Press, New York (2002)
50. Hutchinson, M.D.: Replacing the equations of Fano and Fisher for cased charge blast equivalence—I ductile casings. Propellants Explos. Pyrotech. **36**(4), 310–313 (2011). https://doi.org/10.1002/prep.201000167
51. Houim, R.W., Kuo, K.K.: A low-dissipation and time-accurate method for compressible multi-component flow with variable specific heat ratios. J. Comput. Phys. **230**(23), 8527–8553 (2011). https://doi.org/10.1016/j.jcp.2011.07.031
52. Kim, K.H., Kim, C.: Accurate, efficient and monotonic numerical methods for multi-dimensional compressible flows part I: spatial discretization. J. Comput. Phys. **208**(2), 527–569 (2005). https://doi.org/10.1016/j.jcp.2005.02.021
53. Kim, K.H., Kim, C.: Accurate, efficient and monotonic numerical methods for multi-dimensional compressible flows part II: multi-dimensional limiting process. J. Comput. Phys. **208**(2), 570–615 (2005). https://doi.org/10.1016/j.jcp.2005.02.022
54. Harten, A., Lax, P.D., Leer, B.: On upstream differencing and Godunov-type schemes for hyperbolic conservation laws. SIAM Rev. **25**(1), 35–61 (1983). https://doi.org/10.1137/1025002
55. Toro, E.F., Spruce, M., Speares, W.: Restoration of the contact surface in the HLL-Riemann solver. Shock Waves **4**(1), 25–34 (1994). https://doi.org/10.1007/BF01414629
56. Shen, Z., Yan, W., Yuan, G.: A robust HLLC-type Riemann solver for strong shock. J. Comput. Phys. **309**, 185–206 (2016). https://doi.org/10.1016/j.jcp.2016.01.001
57. Spiteri, R.J., Ruuth, S.J.: A new class of optimal high-order strong-stability-preserving time discretization methods. SIAM J. Numer. Anal. **40**(2), 469–491 (2003). https://doi.org/10.1137/S0036142901389025
58. Zhang, W., Almgren, A., Beckner, V., Bell, J., Blaschke, J., Chan, C., Day, M., Friesen, B., Gott, K., Graves, D., Katz, M.P., Myers, A., Nguyen, T., Nonaka, A., Rosso, M., Williams, S., Zingale, M.: AMReX: a framework for block-structured adaptive mesh refinement. J. Open Source Softw. **4**, 1370 (2019). https://doi.org/10.21105/joss.01370
59. Houim, R.W., Oran, E.S.: Structure and flame speed of dilute and dense layered coal-dust explosions. J. Loss Prev. Proc. **36**, 214–222 (2015). https://doi.org/10.1016/j.jlp.2015.01.015
60. Houim, R.W., Oran, E.S.: Numerical simulation of dilute and dense layered coal-dust explosions. Proc. Combust. Inst. **35**(2), 2083–2090 (2015). https://doi.org/10.1016/j.proci.2014.06.032
61. Houim, R.W., Taylor, B.D.: Detonation initiation from shock and material interface interactions in hydrogen–air mixtures. Proc. Combust. Inst. **37**(3), 3513–3520 (2019). https://doi.org/10.1016/j.proci.2018.06.037
62. Dobratz, B.M.: LLNL explosives handbook: properties of chemical explosives and explosives and explosive simulants. Technical Report, Lawrence Livermore National Lab., CA (USA) (1981)
63. Domalski, E.S., Hearing, E.D.: Condensed phase heat capacity data. In: Linstrom, P.J., Mallard, W.G. (eds.) NIST Chemistry WebBook, NIST Standard Reference Database Number, vol. 69. National Institute of Standards and Technology, Gaithersburg (2021)
64. Brouillette, M.: The Richtmyer–Meshkov instability. Annu. Rev. Fluid Mech. **34**(1), 445–468 (2002). https://doi.org/10.1146/annurev.fluid.34.090101.162238
65. Toro, E.F.: Riemann Solvers and Numerical Methods for Fluid Dynamics, 2nd edn. Springer, New York (1999)